Journal of Hydrology: Regional Studies 68 (2026) 104117

Contents lists available at ScienceDirect

Journal of Hydrology: Regional Studies

journal homepage: www.elsevier.com/locate/ejrh

Attribution of climate and anthropogenic controls on terrestrial water storage changes in the cold and arid regions of the Indus River Basin

Muhammad Adnan [a], Leilei Yong [a], Qiaojuan Xi [a], Muhammad Saifullah [b], Qaisar Saddique [c], Waqas Ul Hussan [d], Hongkai Gao [a,*]

[a] Key Laboratory of Geographic Information Science (Ministry of Education), School of Geographic Sciences, East China Normal University, Shanghai, 200241, China
[b] Department of Agricultural Engineering, Muhammad Nawaz Shareef University of Agriculture, Multan 66000, Pakistan
[c] Potsdam Institute for Climate Impact Research, Member of the Leibniz Association, Telegrafenberg, 14473 Potsdam, Germany
[d] Department of Irrigation and Drainage, University of Agriculture, DI Khan 29111, Pakistan

ARTICLE INFO

Keywords:
Anthropogenic impacts
Climate variability
GRACE/GRACE-FO
Groundwater depletion
Indus River Basin
TWSA

ABSTRACT

Study region: The Indus River Basin (IRB) is a major transboundary river basin in South Asia.
Study focus: The study focuses on quantifying the respective roles of climatic variability and anthropogenic water use in driving terrestrial water storage anomaly (TWSA) decline using a physically informed, decomposition-based attribution framework and spatiotemporal changes in TWSA over the IRB during April 2002–August 2025 using extended GRACE/GRACE-FO data.
New hydrological insights for the region: Trend analysis shows intensification of TWSA decline in humid (-39.8 mm yr^{-1}), semiarid (-34.9 mm yr^{-1}), and cold (-27.4 mm yr^{-1}) regions, while comparatively weak decline in arid (-4.02 mm yr^{-1}) during 2016–2025 as compared to 2002–2015. Signed covariance decomposition identified GWSA as the dominant positive component of TWSA variability (99.9–105.2%), followed by GMB (15.7–18.6%), whereas RZSM, SWE and reconstruction error provided compensating contributions. Basin-scale analysis further shows accelerated groundwater depletion during 2016–2023 (GWS ≈ -13.9 mm yr^{-1}), accompanied by intensified anthropogenic-associated TWSA decline (≈ -16.5 mm yr^{-1}). During 2016–2023, anthropogenic-associated components accounted for the largest relative magnitude shares in arid (59%) and semiarid (67%) regions and across the basin (51%). The climate-related share was largest in the cold region (55%), whereas climate-related and anthropogenic-associated shares were comparable in the humid region (38% and 36%, respectively). These findings highlight the combined influence of human water use and hydroclimatic variability in shaping recent basin-scale water storage decline.

1. Introduction

Freshwater systems globally are undergoing increasing stress driven by intensified climatic variability and growing anthropogenic demand (Haddeland et al., 2014; Vörösmarty and Sahagian, 2000). These pressures are especially acute in arid and semi-arid regions,

* Corresponding author.
E-mail address: hkgao@geo.ecnu.edu.cn (H. Gao).

https://doi.org/10.1016/j.ejrh.2026.104117
Received 9 April 2026; Received in revised form 12 September 2026; Accepted 17 October 2026
Available online 23 October 2026
2214-5818/© 2026 The Author(s). Published by Elsevier B.V. This is an open access article under the CC BY license (http://creativecommons.org/licenses/by/4.0/).

where amplified warming relative to other climatic zones accelerates hydrological depletion and magnifies systemic water scarcity risks (Huang et al., 2017; Cui et al., 2025). This global trend is particularly pronounced in High Mountain Asia (HMA), where human and climate influences are altering water and energy dynamics within a region that is critical for global water resources. Recent assessments, including findings from the IPCC Special Report on the Ocean and Cryosphere in a Changing Climate (SROCC), indicate pronounced reductions in snow cover extent and seasonal persistence at lower elevations, concurrent with accelerating glacier retreat and permafrost degradation in high mountain environments over the past several decades (IPCC, 2022; Wang et al., 2023a,b). However, quantifying water storage and fluxes remains challenging due to large uncertainties in atmospheric inputs and limited constraints on human water extraction (Maina et al., 2024). Consequently, water resource system vulnerability is becoming increasingly evident, particularly in high-altitude catchments where climate change is intensifying cryospheric loss, environmental instability, and socio-economic exposure (Wang et al., 2023a,b).

The IRB represents one of the largest transboundary river systems globally and serves as a primary freshwater source for millions of people across South Asia (Davidson, 2018; Vinca et al., 2021). Its water resources sustain multiple critical sectors, including irrigated agriculture, hydropower generation, tourism, and natural hazard mitigation, making the basin a strategic hydrological system for regional socio-economic development (Immerzeel et al.,A2010; Bocchiola & Soncini, 2019). Snow- and glacier-derived meltwater supports much of the population living within the IRB, yet rising demand and climate-driven cryosphere loss are increasing stress on regional water resources (Dharpure et al., 2025). Recent observations reveal sustained cryospheric degradation, including glacier thinning at an average rate of 0.35 ± 0.33 m yr^{-1} between 2000 and 2012 (Abdullah et al., 2020) and reduced seasonal snow cover from 2008 to 2018 (Ali et al., 2020). These changes have been linked to accelerated TWS decline across the IRB (Zhu et al., 2021). Besides, inconsistent canal water supply has driven extensive dependence on groundwater for irrigation, either as a main source or to buffer surface water shortages. As agricultural pumping has expanded substantially in recent decades (Cheema et al., 2014; Usman et al., 2020), groundwater extraction now exceeds recharge in many areas, resulting in significant aquifer depletion (Lytton et al., 2021).

Quantifying hydrological processes in the IRB remains challenging due to the diverse origins of runoff, including rainfall, snowmelt, glacier melt, and permafrost thaw, as well as the influence of complex topography, monsoon variability, and rapidly changing irrigation demand (Loomis et al., 2019). Advances in satellite gravimetry, particularly with the launch of GRACE in April, 2002, have substantially improved the ability to monitor basin-scale TWSA by providing continuous, large-area mass change measurements (Tapley et al., 2004; Luthcke et al., 2013; Getirana et al., 2025) at roughly 400 km resolution near the equator (Solovey et al., 2025). TWSA encompass all water stored within the landscape, including groundwater storage (GWS), surface water storage (SWS), root zone soil moisture (RZSM), snow water equivalent (SWE), and glacier mass balance (GMB) anomalies, and play a critical role in controlling regional and global water availability (Girotto and Rodell, 2019; Tapley et al., 2019). The GRACE and GRACE-FO missions now offer a unique capability for directly observing TWSA trends at broad spatial scales, complementing and, in many cases, replacing traditional in situ monitoring approaches (Velicogna et al., 2014; Tapley et al., 2019). It offers a valuable insight into how water storage varies across space and time (Dharpure et al., 2025). Changes in TWSA can amplify hydrological extremes such as droughts and floods (Lopez et al., 2020), modulate global sea-level fluctuations through redistribution of continental water mass (Eicker et al., 2016), and remain closely linked to cryospheric mass variations in glaciers and ice sheets (van den Broeke et al., 2009; Tapley et al., 2019). Temporal fluctuations in TWSA reflect the net interaction among precipitation, evaporation, and runoff, thereby integrating the combined effects of climate variability, long-term climatic shifts, and anthropogenic water use on regional hydrological dynamics (Solovey et al., 2025). More recently, GRACE-derived TWSA estimates have also been recognized as a useful tool to assess the groundwater storage variability in regions lacking sufficient in situ monitoring networks (Akhtar et al., 2022).

The IRB exhibits substantial spatial and temporal heterogeneity in TWSA variability, however, previous studies have largely examined basin-scale TWSA variability (e.g., Loomis et al., 2019; Mehmood et al., 2022; Akhtar et al., 2022), whereas comparatively less attention has been given to its spatial heterogeneity, long-term trends, and the relative contributions of climate-related and anthropogenic-associated factors across different hydroclimatic regions of the IRB (e.g., Zhu et al., 2021; Arshad et al., 2024; Dharpure et al., 2025). Their assessments have largely relied on comparing TWSA and GWS variations between the glaciated and non-glaciated regions of the IRB to infer climatic-related and anthropogenic-associated influences. As, the IRB encompasses diverse hydroclimatic regions, the dominant controls on TWSA are likely to vary spatially. Therefore, basin-wide or spatially limited assessments may not fully capture regional differences in the effects of climatic variability and human activities on TWSA across the basin. Previous studies have also provided limited annual and seasonal assessments of the contributions of GWS, RZSM, SWE, GMB, and SWS to TWSA variability, including their spatial dominance across the IRB (e.g., Loomis et al., 2019; Mehmood et al., 2022; Akhtar et al., 2022; Arshad et al., 2024; Dharpure et al., 2025). Because TWSA and its constituent storage components vary seasonally and spatially, neglecting these patterns may obscure changes in the dominant storage component and its influence on TWSA across the basin.

Based on above mentioned research gaps, this study addresses the following research questions: (i) How do TWSA and its major water storage components vary spatially and temporally across different hydroclimatic regions of the IRB? (ii) How do the variability magnitude and signed covariance contribution of individual water-storage components to TWSA vary spatially and seasonally across the hydroclimatic regions of the IRB? (iii) What are the relative contributions associated with climate-related variability and anthropogenic influences to TWSA variations across different hydroclimatic regions of the IRB?

This study provides a spatially explicit and seasonally resolved assessment of TWSA and its major storage components across the hydroclimatic regions of the IRB. Rather than relying solely on the conventional glaciated and non-glaciated classification of the IRB, this study investigates the spatial and temporal differences in storage components dominance and quantifies the relative roles of climatic-related and anthropogenic-associated controls on TWSA variability using a physically informed statistical framework. Compared with empirical-based approaches (e.g., Arshad et al., 2024; Dharpure et al., 2025; Yan et al., 2025), this decomposition-based method provides a more robust and physically interpretable separation of controls on TWSA variability. By

resolving the timing, magnitude, and spatial distribution of climatic-related and anthropogenic-associated influences, the analysis provides an improved diagnostic basis for understanding TWSA dynamics and supports evidence-based groundwater management, irrigation planning, and climate adaptation in this vulnerable basin.

2. Materials and methods

A summary of the complete analytical workflow and the purpose of each method is provided in Supplementary Fig. S1. Detailed descriptions of the study area, datasets, and analytical methods are presented below.

2.1. Study area

The IRB spans multiple countries in South Asia, with headwaters on the Tibetan Plateau near Mount Kailash and Lake Mansarovar, and drains southward to the Arabian Sea (Fig. 1). Approximately 47% of the Indus drainage area falls within Pakistan, with the remainder distributed across India (39%), China (8%), and Afghanistan (6%). The IRB extends between latitudes 23.5°N–37.5°N and longitudes 66°E–82.5°E, covering a drainage area of roughly 1116,000 km^2 and providing water to an estimated 300 million people (FAO, 2011; Laghari et al., 2012; Arshad et al., 2024). Basin elevations range from sea level at the Arabian Sea outlet to approximately 8600 m at the highest peaks of the Karakoram Range. The Jhelum, Chenab, Ravi, Beas, and Sutlej are the principal tributaries of the IRB.

The IRB comprises four major climatic zones: arid (36%), semi-arid (25%), dry sub-humid & humid (16%), and cold (23%), as classified following the United Nations Environment Programme (UNEP) aridity framework using precipitation and potential evaporation data (Fig. 2a). Rainfall in the basin occurs primarily during the summer due to the monsoon and in winter due to westerly disturbances. Mean annual precipitation varies across these climate zones: 100–250 mm in the arid zone, 250–500 mm in the semi-arid zone, and 500–1500 mm in the humid zone, while the cold region exhibits high spatial variability, ranging from less than 100 mm to over 1500 mm (Immerzeel et al., 2010). Total annual potential evaporation across the IRB ranges from 60 to 1800 mm (Dars et al., 2017).

The IRB and its adjoining streamflows are mainly influenced by snow and glacier melt sourced in the cold regions. The glacier-

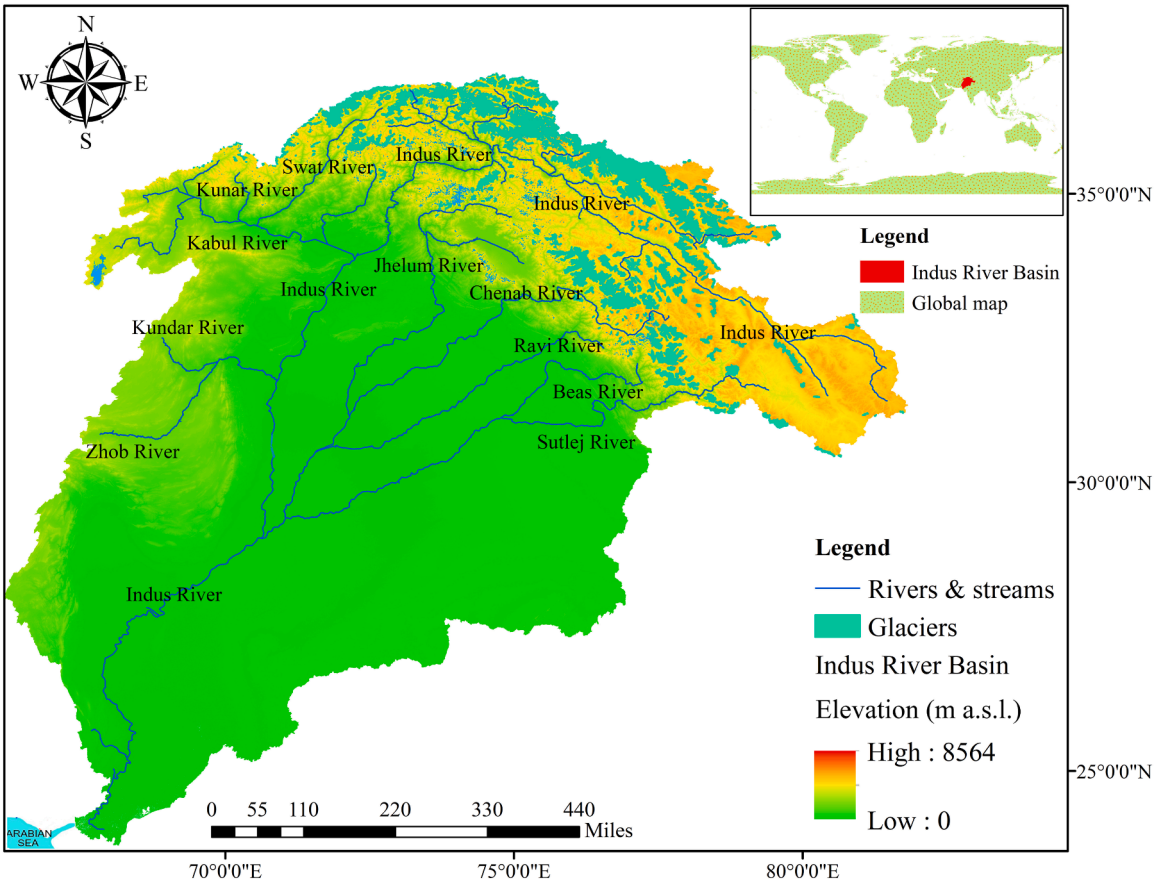


Fig. 1. Geographical location of Indus River Basin.

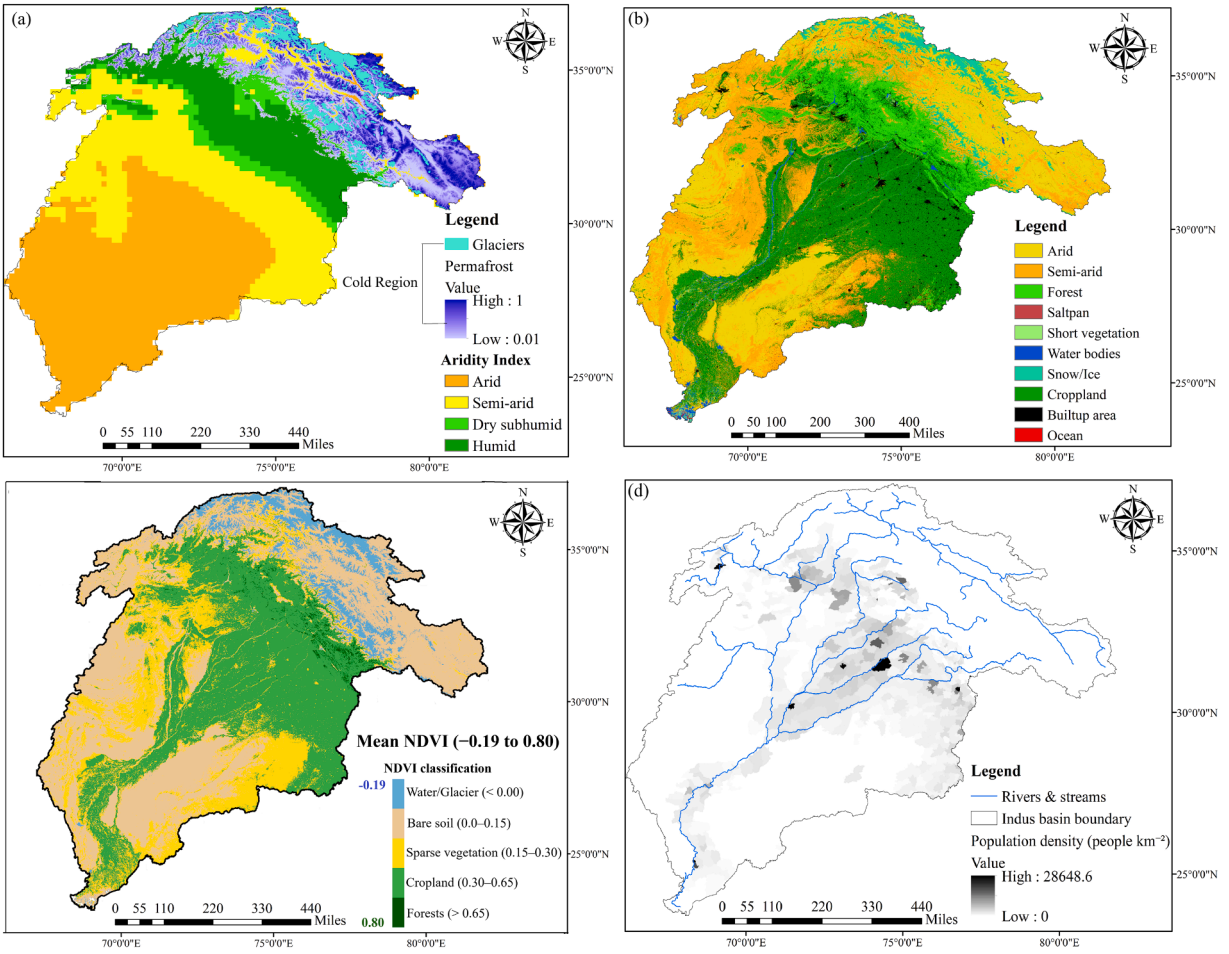


Fig. 2. (a) UNEP aridity index (AI = P/PET) classification, (b) Land-use classification, (c) Normalized Difference Vegetation Index (NDVI), (d) Population density map.

covered area of the Upper Indus Basin (UIB) is estimated at 21,500 km^2. In the UIB, 70–80% of streamflow is supplied by snow and glacier melt, playing a crucial role in supporting lowland agricultural systems (Lutz et al., 2016). The dominant land-use type in the IRB is irrigated agriculture, covering 27% of the basin (Fig. 2b). The mean Normalized Difference Vegetation Index (NDVI) over the IRB during 2001–2024 spans from −0.19 to 0.80, with negative values representing non-vegetated surfaces such as water bodies and areas covered by snow and glaciers in the upper basin, and barren or desert terrain in arid downstream areas, while higher positive values reflect dense and healthy vegetation (Fig. 2c). Arid regions are characterized by a mosaic of agricultural land and desert surfaces, whereas semi-arid areas are predominantly occupied by agricultural croplands. In contrast, humid zones are dominated by dense vegetation and forest cover, while cold regions are characterized by sparse vegetation. The population density map (Fig. 2d) shows that most of the basin's population resides in the arid to semi-arid zones adjacent to the Indus River and its tributaries, with densities ranging from 0 to 28,648 people per km^2.

2.2. Datasets

2.2.1. Topographic data

The IRB was delineated using ASTER-GDEM Version 3, which provides a 30 m spatial resolution. Land-use data at 30 m resolution were obtained from the Global Land Analysis and Discovery (GLAD) database for the year 2019. The global dataset is provided in 10° × 10° tiles, with each tile distributed as two separate GeoTIFF files. For this study, six GeoTIFF tiles were utilized to extract land-use information across the IRB.

Glacier outlines were sourced from the Randolph Glacier Inventory (RGI) Version 7.0 in vector format and subsequently processed in ArcGIS to quantify glacier extent within the basin. Permafrost zonation index data at < 1 km spatial resolution, sourced from Gruber (2012), were used to map and visualize permafrost distribution within the IRB (Fig. 2).

Normalized Difference Vegetation Index (NDVI) data at 250 m spatial resolution and 16-day temporal intervals for 2001–2024 were sourced from the MODIS Terra Vegetation Indices product (MOD13Q1, Version 6.1). These data were subsequently processed to

derive basin-wide mean NDVI values for the IRB. In addition, the study used 2020 population data from GPWv4 (1 km spatial resolution), sourced from the United States Geological Survey (USGS) and NASA Earth Data (Table 1).

2.2.2. Hydro-climatic data

Precipitation, temperature, evaporation, and runoff data for 2002–2023 were obtained from ERA5-Land (Copernicus Climate Change Service (C3S), 2025) and used to support the attribution of GRACE-derived TWSA across the IRB (Table 1).

2.2.3. Terrestrial water storage and ancillary datasets

2.2.3.1. GRACE CSR Mascon. The GRACE CSR Mascon TWSA product (RL06; Save et al., 2016; Save, 2020; Center for Space Research (CSR), University of Texas at Austin, 2025), provided at 0.25° spatial resolution, was used to analyze TWSA over the IRB for April 2002–August 2025 (Table 1). However, this grid spacing does not represent the effective spatial resolution of GRACE/GRACE-FO. The gridded values are an oversampled representation of the underlying gravity-field solution and should not be regarded as independent observations at each grid cell. Monthly anomalies are referenced to the 2004–2009 baseline period. In the CSR RL06 framework, mass changes are estimated on an ellipsoidal Earth and include land–ocean leakage corrections to reduce signal contamination (Ditmar, 2018). The dataset also incorporates Glacial Isostatic Adjustment corrections to remove long-term crustal deformation unrelated to contemporary hydrological processes. Owing to these methodological improvements, the CSR RL06 mascon product was selected to

Table 1
Summary of datasets, characteristics, and their roles in the present analysis.

Dataset	Variable (s)	Spatial resolution	Temporal resolution	Study period	Role in this study	Source
ASTER GDEM	Elevation	30 m	Static	2019 release	Basin topography, elevation analysis, and map preparation	J-spacesystems
Global land-use	Land-use classes	30 m	Static	2019	Characterization of land-use patterns	GLAD/UMD
Randolph Glacier Inventory v7.0	Glacier outlines	vector	Static	2023 release	Delineation of glacierized areas	GLIMS/RGI
MOD13Q1	NDVI	250 m	16-day	2001–2024	Vegetation predictor in the attribution analysis	NASA MODIS
GPWv4	Population count/density	1 km	Static	2020	Contextual assessment of population distribution; not used as a direct attribution predictor	NASA SEDAC
Global permafrost	Permafrost extent	< 1 km	Static	2012	Characterization of cold-region surface conditions	Gruber, (2012)
ERA5-Land	Precipitation, temperature, evapotranspiration, runoff	0.10°	Monthly after aggregation	2002–2023	Climate-related predictors used in driver attribution	Copernicus Climate Data Store
GRACE CSR mascon RL06	TWSA	0.25° grid spacing	Monthly	2002–2025	Primary dataset for TWSA trends, change-point analysis, decomposition, and attribution	CSR/UT Austin
GLDAS-CLSM v2.2	Land-surface water-storage components	0.25°	Daily, aggregated monthly	2002–2023	Estimation of non-groundwater storage components used in residual GWSA derivation	NASA GES DISC
GravIS	RZSM, SWE, GMB, and SWS	0.50°	Monthly	2002–2023	Storage-component analysis, GWSA derivation, and zone-specific predictor construction	GFZ GravIS
G3P-GWS	Groundwater-storage anomaly	0.50°	Monthly	2002–2023	Independent comparison or sensitivity assessment of groundwater-storage variability	GFZ
GTWS-MLrec	Reconstructed TWSA	0.25°	Monthly	2002–2022	Reconstruction of missing GRACE months	Yin et al. (2023) dataset
Groundwater monitoring wells	Groundwater level	Point observations	Biannual	2002–2024	Validation of GRACE-derived GWSA and assessment of local groundwater-level variability	IGRAC/CGWB
WaterGAP v2.2e	Potential groundwater withdrawals for irrigation (PIRRWWGW)	0.50°	monthly	2002–2023	Predictor representing groundwater demand for irrigation	Müller Schmied et al., (2024)
MIRCA-OS v2	Irrigated growing-area intensity anomaly (dimensionless)	5 arc-minutes (~0.0833°)	Monthly crop calendars at five-year benchmarks	2002–2023*	Predictor representing irrigated crop intensity and seasonality	Kebede et al., (2025)

assess climate-related and human-associated contributions to TWSA variability across the basin. Missing GRACE/GRACE-FO TWSA observations were reconstructed using the CSR-based Global Terrestrial Water Storage Machine Learning Reconstruction dataset (GTWS-MLrec; Yin et al., 2023), as detailed in Supplementary Section S2. Besides, the non-parametric Pettitt test was applied to the monthly GRACE TWSA series for April 2002–August 2025 to detect an abrupt shift in basin-wide storage conditions (Supplementary Section S3; Fig. S3).

2.2.3.2. GLDAS-CLSM. The NASA Global Land Data Assimilation System (GLDAS; Rodell et al., 2004) provides daily TWS estimates at 0.25° resolution, which were analyzed alongside the GRACE CSR mascon dataset for climate-related and anthropogenic-associated attribution. GLDAS data were resampled to a common grid, aggregated to monthly means, and converted to anomalies using a consistent baseline period (2004–2009).

GLDAS-CLSM v2.2 (NASA Goddard Earth Sciences Data and Information Services Center (GES DISC), 2025) was used to provide land-surface water storage components required for GRACE-based TWSA partitioning. GLDAS products have been widely applied in GRACE hydrological studies, including assessments in the IRB using GLDAS-NOAH estimates of SM and SWE anomalies (Akhtar et al., 2022; Mehmood et al., 2022). GLDAS-CLSM v2.2 product was selected because it provides spatially and temporally consistent estimates of water-storage components and includes GRACE-based data assimilation. However, this assimilation introduces partial dependence between GLDAS-derived variables and GRACE observations; therefore, these variables are treated as model-based estimates rather than independent observations. In GLDAS, total TWS is composed of canopy water storage (CWS), soil moisture (SM) and snow water equivalent (SWE), and thus predominantly captures climate-related variations in land water storage, while excluding direct representations of anthropogenic groundwater abstraction.

2.2.3.3. GravIS. Time series of storage component anomalies, including RZSM (Pasik et al., 2023), SWE (Luojus et al., 2021), GMB, and SWS (Prudhomme et al., 2024), were obtained from the Gravity Information Service (GravIS; Dahle et al., 2025). These monthly gridded datasets span February 2002 to September 2023 at 0.5° spatial resolution and were resampled to the GRACE grid for spatial consistency. All anomaly fields were referenced to long-term monthly means over April 2002–March 2020. GravIS was selected primarily because of its temporal coverage, monthly resolution, and consistent provision of the storage components required for the analysis. GravIS components were evaluated using unscaled mean absolute deviation to quantify variability magnitude and signed covariance decomposition to assess their spatial and temporal contributions to GRACE-derived TWSA variability.

2.2.3.4. G3P-GWS. The Global Gravity-based Groundwater Product (G3P; Güntner et al., 2024) provides groundwater storage anomalies by integrating GRACE-derived TWSA observations with complementary water storage components available within the Copernicus data portfolio. In this framework, GWS anomalies are estimated by subtracting RZSM, GMB, SWE, and SWS components from the GRACE TWSA signal. This approach enables the isolation of groundwater variability that is not explicitly represented in conventional land surface models.

2.2.3.5. Irrigation activity proxies. Monthly potential groundwater withdrawals for irrigation (PIRRWWGW) during 2002–2023 were obtained from WaterGAP v2.2e simulations driven by GSWP3–ERA5 climate forcing (Müller Schmied et al., 2024). The data were clipped to the Indus River Basin boundary, resampled from 0.5° to the 0.25° GRACE analysis grid, and converted to consistent units for use as a proxy for irrigation demand. MIRCA-OS irrigated areas (Kebede et al., 2025) were summed across crops, masked to the study region and aggregated to the 0.25° GRACE grid, then normalised by masked cell area. Monthly intensities for April 2002–September 2023 were linearly interpolated by calendar month between five-year benchmarks (2000–2020), with the 2020 pattern repeated for 2021–2023. Each cell's overall 2004–2009 mean was subtracted to obtain anomalies while retaining seasonality. These datasets were subsequently used as predictors in the GRACE TWSA attribution framework.

2.2.4. Groundwater monitoring wells data

Groundwater observations were obtained from the International Groundwater Resources Assessment Centre (IGRAC) groundwater monitoring database, including records contributed by the Central Ground Water Board (CGWB), India. A total of 3336 monitoring wells with long-term records (2004–2024) were selected from regions exhibiting pronounced groundwater depletion across the IRB (Supplementary Section S4, Fig. S4).

The dataset provides biannual groundwater level measurements referenced to ground surface, corresponding to pre-monsoon (May) and post-monsoon (November) conditions. Groundwater storage change at each well was estimated using the water table fluctuation method:

$$\Delta S_{obs} = \left(h_{pre} - h_{post}\right) \times S_y \tag{1}$$

Where h_{pre} and h_{post} denote pre- and post-monsoon depth to water, respectively, and S_y is specific yield, and ΔS_{obs} represents groundwater storage change derived from well observations. Positive values indicate groundwater recharge (rise in water table), whereas negative values indicate depletion. A uniform specific yield ($S_y = 0.12$) representative of the Indo-Gangetic Plain was adopted following previous studies (e.g., Iqbal et al., 2016; MacDonald et al., 2016; Bhanja et al., 2016; Arshad et al., 2024) and regional hydrogeological assessments (e.g., Central Ground Water Board, 2013; Central Ground Water Board, 2017), where typical values for alluvial aquifers range between 0.08 and 0.15. This approach was used due to the lack of spatially distributed estimates across the study region.

Groundwater storage was converted to anomalies ($GWSA_{wells}$) by removing the mean over the 2004–2009 baseline period, consistent with GRACE-based estimates. Seasonal groundwater storage change from GRACE was computed as post-monsoon minus pre-monsoon anomalies to ensure consistency in sign interpretation with observation-based estimates. To reduce the scale mismatch between point-based observations and gridded GRACE data, a circular buffer was defined around each well, and the mean GWSA of all grid cells within the buffer was assigned to that location. This buffer-averaging approach provides a more representative comparison with the spatially integrated satellite signal.

2.3. Methods

2.3.1. Trend detection and magnitude estimation

The non-parametric Mann–Kendall (MK) test (Mann, 1945; Kendall, 1957) was employed to detect statistically significant monotonic trends in GRACE-derived TWSA. The same approach was applied within the attribution framework to quantify trends in GWSA and in the decomposed climate-driven and anthropogenic components of TWSA. At the grid-cell scale, the spatial distribution of trends was evaluated using the MK test, and for statistically significant grid cells ($p < 0.05$), trend magnitudes were quantified using Sen's slope estimator (Sen, 1968; Ali et al., 2022; Wang et al., 2023a,b), which yields a reliable estimate of the median change rate. Trend analysis was performed on deseasonalized monthly GRACE TWSA, with time expressed as fractional years, and all trends are reported as annual rates (mm yr^{-1}). For regional-scale analysis, basin-averaged time series were obtained by averaging values across all grid cells within the basin, and trends and their magnitudes were assessed, employing the MK test alongside Sen's slope estimator, respectively. These non-parametric methods were selected for their robustness to outliers, missing values, and non-normal data distributions frequently observed in hydrological and climate time series (Cao et al., 2025; Cui et al., 2025).

2.3.2. Mean absolute deviation and covariance-based storage contribution analysis

GRACE-derived TWSA represents the combined variability of multiple TWSA components, including GWS, RZSM, SWE, GMB, and SWS. Spatial variability and component contributions were assessed from temporally aligned GRACE and GravIS anomaly datasets. Unscaled mean absolute deviation (MAD) quantified the variability magnitude of TWSA and its storage components (Feng et al., 2020; Ning et al., 2023), whereas signed contributions were estimated by normalizing each component's covariance with TWSA by the variance of TWSA (Chao et al., 2023; Lee et al., 2023). At the annual scale, MAD was computed using all 12 monthly anomalies within each year, while at the seasonal scale, MAD was calculated from the corresponding three-month seasonal anomalies. The component MAD values were not rescaled to match the TWSA MAD, and the residual reconstruction error was retained to represent component inconsistencies and unexplained variability.

The MAD of GRACE-derived TWSA was computed by Eq. 2 given below:

$$MAD_{TWSA} = \frac{1}{n}\sum_{t=1}^{n} |TWSA \quad (t) - \overline{TWSA}| \tag{2}$$

Where $TWSA(t)$ represents the GRACE-derived anomaly at time step t (months), while $\overline{TWSA}$ denotes mean TWSA over the study period. MAD_{TWSA} provides the average absolute deviation in millimeters, representing the magnitude of variability.

Similarly, the MAD of each storage component anomaly (C_j), was calculated using Eq. (3).

$$MAD(C_j) = \frac{1}{n}\sum_{t=1}^{n} \left|C_j(t) - \overline{C}_j\right| \tag{3}$$

Here, C_j represents GWS, RZSM, SWE, GMB, and SWS. These unscaled MAD values, expressed in millimeters, quantify the variability of each storage component and are not treated as additive.

The signed contribution of each storage component (j) to TWSA variability was estimated using the covariance-based expression (Eq. 4).

$$Contribution_j(\%) = \frac{Cov\left(C_j, TWSA\right)}{Var(TWSA)} \times 100 \tag{4}$$

Positive values indicate that a component reinforces TWSA variability, whereas negative values denote compensating behavior. As signed covariance shares, contributions may be negative or exceed 100% when strong compensation occurs among storage components.

The difference between GRACE TWSA and the sum of the individual storage components was retained as the reconstruction error as shown in Eq. 5.

$$\varepsilon(t) = TWSA(t) - \sum_{j=1}^{m} C_j(t) \tag{5}$$

The covariance contribution of the reconstruction error was also calculated in the same manner. Consequently, the covariance contributions of all storage components and the reconstruction error sum to 100%.

2.3.2.1. GWSA-exclusion sensitivity analysis. Because GWSA was derived residually from GRACE TWSA, its covariance contribution

was interpreted as a model-derived groundwater signal. Robustness was assessed by excluding GWSA from the reconstruction and comparing the results with independent groundwater observations.

$$R_{-GWS}(t) = TWSA(t) - \sum_{j \neq GWS} C_j(t) \tag{6}$$

Where $R_{-GWS}(t)$ is the residual TWSA after excluding GWS anomaly, $TWSA(t)$ is the GRACE-derived TWSA, and $C_j(t)$ represents the *jth* non-groundwater storage component anomaly at time step *t*. Because MAD is non-additive, the residual was calculated before estimating MAD as shown in Eq. 7.

$$MAD\left(TWSA - \sum_{j=1}^{m} C_j\right) \neq MAD(TWSA) - \sum_{j=1}^{m} MAD(C_j) \tag{7}$$

2.3.3. Derivation of groundwater storage anomalies from GRACE-derived TWSA

GRACE-derived TWSA represents the combined variations of all major water storage components (Tapley et al., 2019; Girotto and Rodell, 2019; Akl et al., 2025). In contrast, GLDAS-derived TWSA includes only soil moisture (SM), snow water equivalent (SWE), and canopy water storage (CWS) anomalies, while SWS and GMB anomalies were obtained from GravIS data. The GLDAS and GravIS storage components were resampled to match the spatial resolution of GRACE and converted to anomalies over the 2004–2009 period, consistent with the GRACE baseline. GWS anomalies were then computed from April 2002 to September 2023 by subtracting the GLDAS and GravIS components from GRACE-derived TWSA using Eq. 8.

$$GWS(t) = TWSA_{GRACE}(t) - SM_{GLDAS}(t) - SWE_{GLDAS}(t) - CWS_{GLDAS}(t) - GMB_{GravIS}(t) - SWS_{GravIS}(t) \tag{8}$$

The GWS derived from Eq. 8 represents total groundwater variability, reflecting the combined effects of climate-related recharge processes and anthropogenic-associated groundwater abstraction. It refers to the estimated GWS anomaly as a GRACE-constrained, model-assisted estimate rather than a fully independent observation. The resulting GWS anomaly time series was subsequently decomposed using Seasonal–Trend decomposition using Loess (STL) and attributed using lagged elastic net regression with blocked time-series cross-validation to separate climate-related and anthropogenic-associated groundwater storage components. These components were then used to facilitate the decomposition of GRACE-derived TWSA into climate-related and anthropogenic-associated contributions across the hydroclimatic regions of the IRB.

2.3.3.1. GRACE-derived groundwater drought index. The GRACE-based Groundwater Drought Index (GGDI) (Thomas et al., 2017) was used to assess and quantify groundwater drought across the IRB. To account for seasonal effects, long-term monthly averages were calculated and subtracted from the GWS, producing the Groundwater Storage Deviation (GSD), which reflects the net seasonal fluctuations in groundwater storage. The GSD was then standardized to derive the GGDI using the following equation:

$$GGDI_t = \frac{GSD_t - \overline{X_{GSD}}}{\sigma_{GSD}} \tag{9}$$

Here, t represents time, while $\overline{X_{GSD}}$ and σ_{GSD} denote the mean and standard deviation of the GSD time series, respectively. A groundwater drought event is considered to start when GGDI remains below zero for at least three consecutive months and is regarded as ended when GGDI stays at or above zero for three consecutive months.

2.3.4. STL–decomposition and attribution framework

2.3.4.1. STL decomposition of GRACE-derived TWSA. The Seasonal–Trend decomposition using Loess (STL) method (Cleveland et al., 1990) was applied to decompose GRACE-derived TWSA into seasonal, long-term, and sub-seasonal components at each grid cell (Humphrey et al., 2016; Scanlon et al., 2018; Yan et al., 2025). The monthly time series is expressed as:

$$TWSA(t) = T_{longterm}(t) + T_{seasonal}(t) + T_{subseasonal}\ (t) \tag{10}$$

The long-term component was further separated into a linear trend and an **interannual variability** using the Theil–Sen estimator (Humphrey et al., 2016, 2017; Scanlon et al., 2018; Zhu et al., 2021):

$$T_{longterm}(t) = T_{linear}(t) + T_{interannual}(t)$$

Therefore,

$$TWSA(t) = T_{linear}(t) + T_{interannual}(t) + T_{seasonal}(t) + T_{subseasonal}\ (t) \tag{11}$$

2.3.4.2. Attribution framework. Long-term storage changes may arise from persistent processes such as groundwater depletion and glacier mass loss, whereas short-term anomalies are often associated with atmospheric forcing, including precipitation and evapotranspiration (Chen et al., 2016; Velicogna et al., 2014; Humphrey et al., 2016). However, temporal scale alone is insufficient to identify the underlying driver. Seasonal and interannual variability is commonly linked to hydroclimatic processes but may also be influenced by irrigation and reservoir regulation. Similarly, the long-term and subseasonal components may contain both

climate-related and anthropogenic-associated signals, with their relative contributions varying among hydroclimatic zones. These influences were therefore evaluated separately through the predictor-based attribution framework.

Accordingly, TWSA was partitioned into three additive components:

$$TWSA_{long}(t) = T_{linear}(t)$$

$$TWSA_{SI}(t) = T_{interannual}(t) + T_{seasonal}(t)$$

$$TWSA_{short}(t) = T_{subseasonal}(t)$$

Where $TWSA_{SI}(t)$ denotes seasonal-interannual variability. Thus,

$$TWSA \quad (t) = \quad TWSA_{long}(t) + TWSA_{SI}(t) + TWSA_{short}(t) \tag{12}$$

2.3.4.3. Lagged elastic net regression with blocked time series cross validation. The long-term, seasonal–interannual and short-term TWSA components were modelled using lagged elastic-net regression (Zou and Hastie, 2005). Regularization stabilized coefficient estimates under multicollinearity, while lags of 0–3 months represented delayed hydrological responses. Model validation used contiguous temporal blocks to account for serial dependence. Predictors were aligned to the GRACE grid and aggregated to basin scale before model fitting.

Predictors were classified into climate-related and anthropogenic-associated variables groups according to their dominant physical interpretation rather than as mutually exclusive causal categories. Climate-related variables included climate-driven groundwater storage (GWSA_CLIM), RZSM, SWE, P, T, ET, runoff, and glacier anomalies, while anthropogenic-associated variables included anthropogenic-induced groundwater storage (GWSA_ANTH), SWS, potential groundwater withdrawals for irrigation (PIRRWWGW), and irrigated growing-area intensity.

The regression model is defined as:

$$Y(t) = \beta_0 + \sum_{k=1}^{p} \beta_k X_k(t) + \epsilon(t) \tag{13}$$

Where $Y(t)$ represents $TWSA_{long}(t)$, $TWSA_{SI}(t)$ or $TWSA_{short}(t)$, $X_k(t)$ are standardized predictors (including lags), and $\epsilon(t)$ is the model residual. Model outputs were partitioned into climatic, anthropogenic, and residual components:

$$Y(t) = \beta_{0,Y} + Y_{clim}(t) + Y_{anth}(t) + \epsilon_Y(t) \tag{14}$$

Where

$$Y_{clim}(t) = \sum_{k \in C} \beta_k X_k(t)$$

$$Y_{anth}(t) = \sum_{k \in A} \beta_k X_k(t)$$

Where C and A represents climate-related and anthropogenic associated predictors groups, respectively.

Accordingly:

$$TWSA_{long}(t) = \beta_{0,long} + TWSA_{long,clim}(t) + TWSA_{long,anth}(t) + \varepsilon_{long}(t)$$

$$TWSA_{SI}(t) = \beta_{0,SI} + TWSA_{SI,clim}(t) + TWSA_{SI,anth}(t) + \varepsilon_{SI}(t)$$

$$TWSA_{short}(t) = \beta_{0,short} + TWSA_{short,clim}(t) + TWSA_{short,anth}(t) + \varepsilon_{short}(t)$$

The total reconstructed climate-related contribution is:

$$TWSA^{total}_{clim}(t) = TWSA_{SI,clim}(t) + TWSA_{long,clim}(t) + TWSA_{short,\quad clim}(t) \tag{15}$$

The anthropogenic-associated contribution is:

$$TWSA^{total}_{anth}(t) = TWSA_{long,anth}(t) + TWSA_{SI,anth}(t) + TWSA_{short,anth}(t) \tag{16}$$

The combined model residual is:

$$\varepsilon_{total}(t) = \varepsilon_{long}(t) + \varepsilon_{SI}(t) + \varepsilon_{short}(t) \tag{17}$$

The combined intercept is:

$$\beta_{0,total} = \beta_{0,long} + \beta_{0,SI} + \beta_{0,short} \tag{18}$$

Therefore, the complete reconstruction is calculated by Eq. 19 given below:

$$TWSA_{recon}(t) = \beta_{0,total} + TWSA^{total}_{clim}(t) + TWSA^{total}_{anth}(t) + \varepsilon_{total}(t) \quad (19)$$

The decomposition was applied at both the hydroclimatic-zone and basin scales, allowing variability at different temporal scales to be represented and subsequently attributed using a separate predictor-based framework. Elastic-net regression was used to assess the joint associations of hydroclimatic and anthropogenic predictors with TWSA components while stabilizing coefficient estimates under multicollinearity. Individual predictor influence was quantified using standardized contributions, and driver-group influence using grouped permutation importance. Details are provided in Supplementary Section S5 and Table S1. The fitted long-term, seasonal-interannual and short-term components were partitioned into climate-related and anthropogenic-associated contributions, with the model intercept retained in the final reconstruction. The remaining difference between each target component and its reconstructed signal was retained as a model residual, reflecting variability not reproduced by the fitted predictors; its magnitude is reported as out-of-fold RMSE per region in Table S2, and it was not assigned to either driver group.

2.3.4.4. Blocked cross-validation. Nested blocked cross-validation used eight outer and four inner contiguous temporal folds, with a three-month exclusion buffer to limit leakage from lagged predictors. Feature screening, imputation and standardization were fitted within outer training sets, and α and λ were tuned through inner validation. Regional performance was evaluated using out-of-fold R^2, RMSE and MAE for each component and the summed TWSA reconstruction. Sensitivity analyses refitted and retuned climate-only and anthropogenic-only models, alongside models excluding GRACE-derived groundwater or surface water storage predictors, with skill compared on identical target months. Residual dependence was assessed using lag-1 autocorrelation of out-of-fold residuals and Ljung–Box tests on continuous monthly segments within held-out folds. Variability not reproduced by the model was retained as an unassigned residual.

2.3.4.5. Relative magnitude share analysis. Relative magnitude shares were quantified using an absolute-magnitude metric, in which the absolute value of each reconstructed component was normalized by the sum of absolute magnitudes of the climate-related, anthropogenic-associated and model residual terms at each time step, excluding the intercept. The resulting shares were then averaged over time to obtain the mean share of each component over the study period.

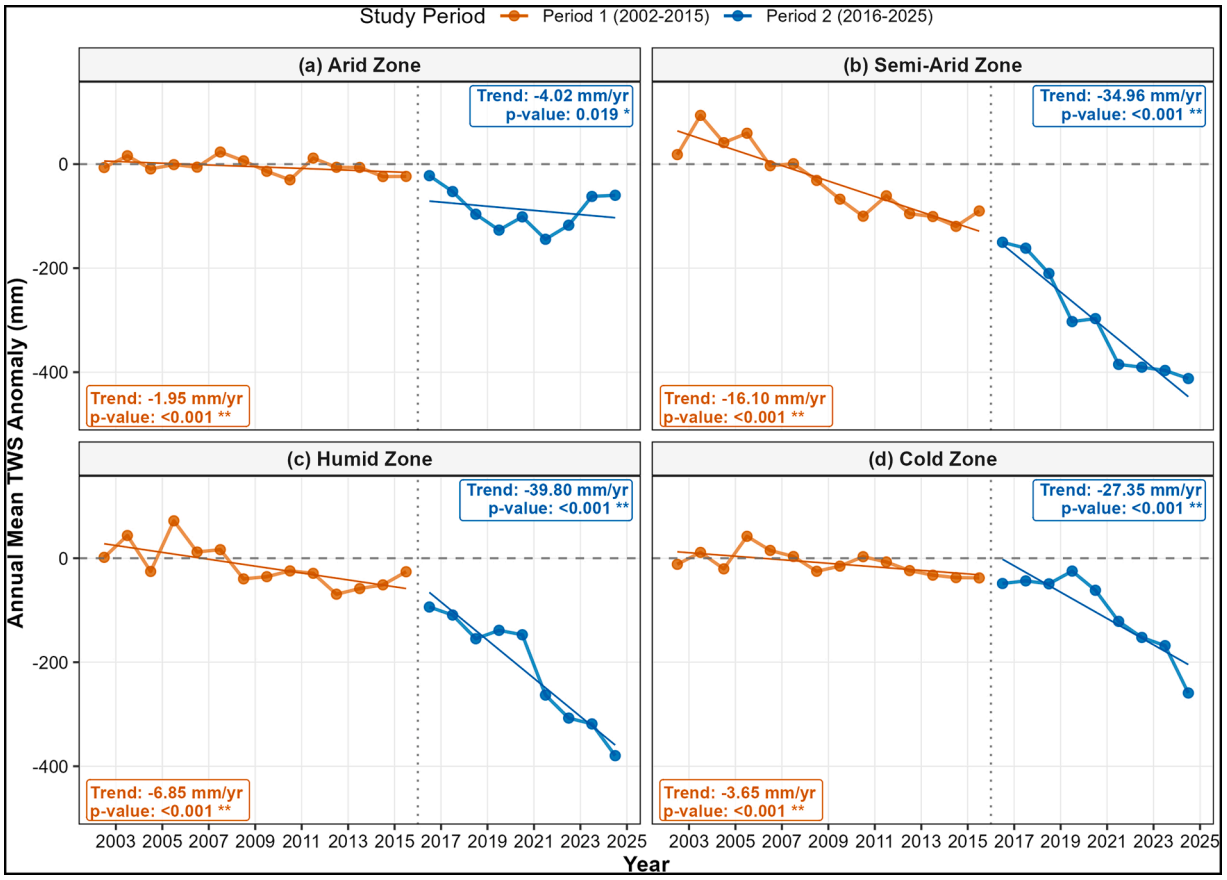


Fig. 3. Temporal variations in GRACE-derived TWSA across major climatic regions (arid, semi-arid, humid, and cold) of the IRB during Period 1 (2002–2015) and Period 2 (2016–2025).

$$c_i(t) = \frac{|TWSA_i(t)|}{\sum_{j=1}^{m} |TWSA_j(t)|} \tag{20}$$

$$C_i = \frac{1}{n} \sum_{t=1}^{n} c_i(t) \tag{21}$$

Where $c_i(t)$ is the relative contribution of component i at time step t, and C_i is the time-averaged contribution over the study period. Because the metric operates on absolute values, it is insensitive to sign and does not account for compensation between components of opposite sign. The resulting values are therefore relative magnitude shares indicating relative influence, and should not be interpreted as fractions of the observed net change in TWSA. The model intercept is excluded from the normalization in Eq. (20).

3. Results

3.1. Temporal dynamics of GRACE-derived TWSA across the hydroclimatic regions of the IRB

Temporal changes in GRACE TWSA across major climatic regions during April 2002–December 2015 and January 2016–August 2025 is presented in Fig. 3. During the first period, the deseasonalized monthly TWSA exhibited a statistically significant declining tendency across all regions, with the strongest depletion observed in the semi-arid zone (−16.1 mm yr^{-1}). This was followed by

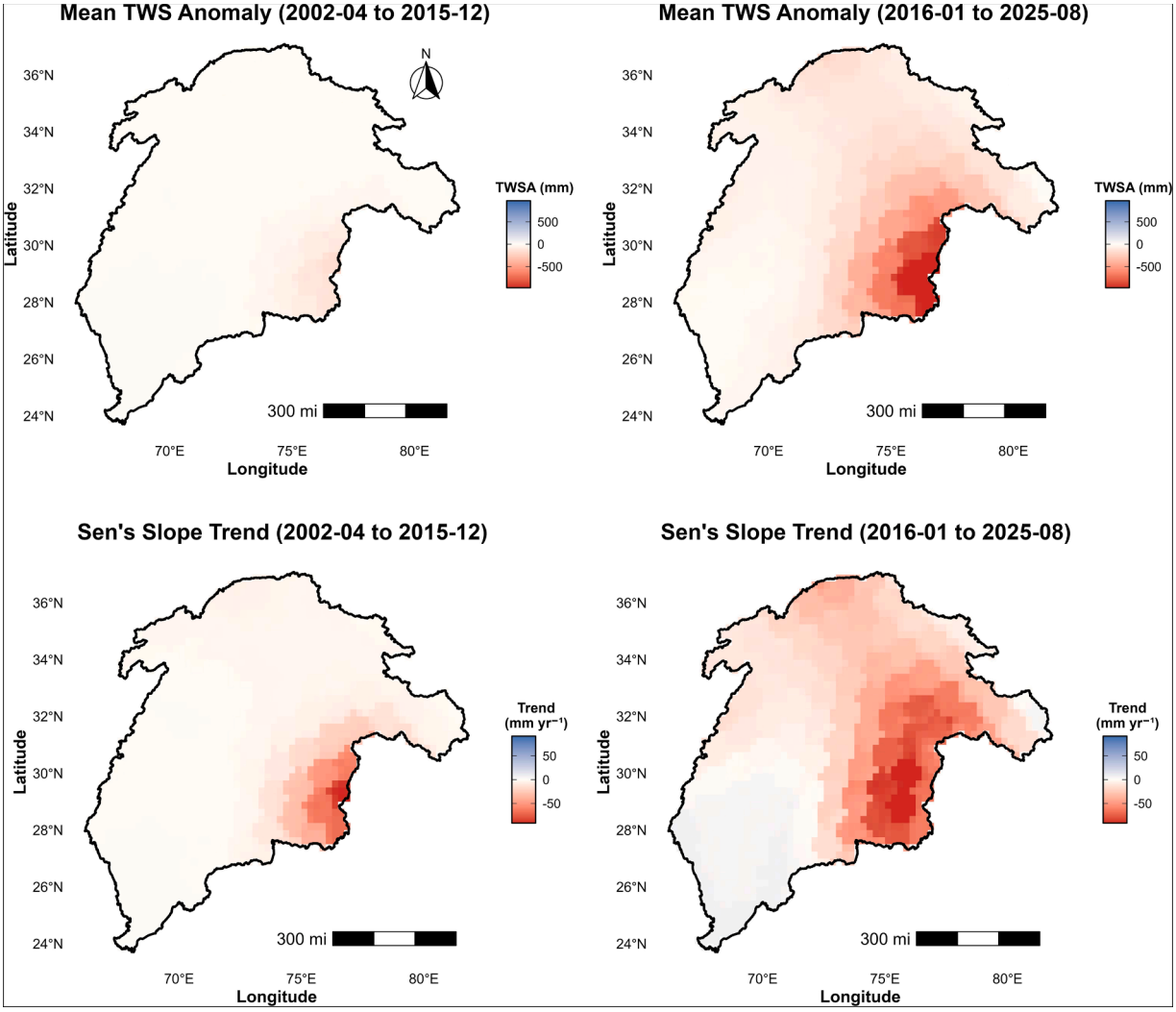


Fig. 4. Spatial patterns and long-term trends of GRACE-derived TWSA over the IRB (2002–2015; 2016–2025), showing mean anomalies as equivalent water height (EWH, mm) and Sen's slope trends (mm yr^{-1}).

moderate declines in the humid (−6.85 mm yr^{-1}) and cold (−3.65 mm yr^{-1}) regions, while the arid region showed a comparatively weaker negative trend (−1.95 mm yr^{-1}).

During the second period, TWSA declines intensified across the basin, indicating a clear shift in hydrological dynamics. The semi-arid region remained a hotspot of depletion (−34.96 mm yr^{-1}), while even stronger declines emerged in humid (−39.80 mm yr^{-1}) and cold regions (−27.35 mm yr^{-1}), highlighting a spatial expansion of severe losses beyond traditionally water-stressed areas. Overall, results reveal a progressive amplification and propagation of TWS depletion from semi-arid to humid and cold regions. In contrast, the arid region showed a transition from earlier decline to a modest post-2021 recovery, whereas other regions continued to exhibit persistent and increasing storage deficits.

3.2. Spatial variability and multi-year trends of GRACE TWSA

Spatial analysis of GRACE-derived TWSA shows a marked increase in storage depletion across the IRB over time as shown in Fig. 4. Area-weighted basin estimates indicate that mean TWSA declined from −13.7 mm during 2002–2015 to −168.6 mm during 2016–2025, reflecting substantially greater water loss in the later period. Likewise, the basin-scale Sen's slope intensified from −6.5 mm yr^{-1} in 2002–2015 to −22.5 mm yr^{-1} in 2016–2025.

The spatial extent of TWSA depletion evolved markedly over time. Before 2015, declines were largely confined to semi-arid regions, whereas after 2015, pronounced losses expanded into humid and cold zones, where the strongest negative trends occurred. In contrast, arid regions exhibited a distinct response, with sustained depletion until 2021 followed by a net recovery during 2022–2025, likely driven by enhanced groundwater recharge from recurrent monsoon flooding, particularly the extreme 2022 event (Fig. 4).

3.3. Annual and seasonal storage contributions to TWSA variability

Basin-scale covariance decomposition identified GWS anomalies as the dominant positive component associated with annual TWSA variability, contributing 103.9% (Table 2). GMB contributed 17.7%, whereas RZSM (−10.7%), SWE (−1.3%), SWS (−0.07%), and the reconstruction error (−9.5%) acted as compensating terms, yielding a net contribution of 100%. The contribution exceeding 100% reflects covariance compensation among storage components rather than an independently explained fraction of TWSA variability.

GWS anomalies remained dominant across all seasons, contributing 99.9% in MAM and 105.2% in SON (Table 2). GMB anomalies accounted for 15.7–18.6%, with the highest value in SON, whereas RZSM anomalies showed compensating contributions of −4.0% to −11.4%. SWE anomalies contributions were small and changed sign seasonally, while SWS anomalies remained negligible. The reconstruction error contributed −9.0% to −11.0%, partly offsetting the excess positive covariance of the storage components.

The spatial patterns were consistent with the basin-scale decomposition (Fig. 5). GWS showed widespread positive contributions, whereas RZSM varied regionally, with positive effects in the western basin and compensating effects in parts of the northern and eastern IRB. SWE and GMB contributions were concentrated in the upper cryospheric region, while SWSA remained minor. Reconstruction error displayed mixed spatial patterns, reflecting regional mismatches between GRACE TWSA and the summed components. As GWS anomalies were derived residually, its dominant contribution represents a model-derived association rather than an independent causal effect.

Unscaled MAD maps showed that GWSA most closely matched the magnitude and broad spatial pattern of TWSA variability, whereas the remaining storage components exhibited much lower variability (Supplementary Section S6, Fig. S5). These values describe variability magnitude and are not treated as additive contributions.

Because GWSA is calculated by subtracting non-groundwater storage components from GRACE TWSA, the resulting water-balance residual is GWSA by definition. This analysis therefore describes an accounting partition rather than independent evidence of groundwater influence. The residual accounts for 97.2% of annual TWSA mean absolute deviation and 92.9–101.2% seasonally, while the non-GWS reconstruction explains 7.9–30.2% of seasonal variance. Thus, the modelled soil moisture, snow and surface water components reproduce only a limited part of observed TWSA variability. The signed covariance decomposition assigns annual shares of 103.9% to GWSA and −9.5% to reconstruction error (Table 2); shares above 100% reflect compensation among oppositely signed terms. These accounting relationships do not establish the residual's physical origin: it contains any groundwater signal together with GRACE measurement and leakage errors and uncertainties in the reconstructed non-GWS components.

Table 2
Annual and seasonal signed covariance contributions of storage components and reconstruction error to basin-mean GRACE-derived TWSA variability in the IRB (values in %).

Period	GWS	RZSM	SWE	GMB	SWS	Error
Annual (J-D)	103.9	-10.7	-1.3	17.7	-0.1	-9.5
Winter (DJF)	103.2	-11.4	1.4	15.7	0.04	-9.0
Spring (MAM)	99.9	-4.0	-1.5	15.7	0.2	-10.3
Summer (JJA)	100.1	-8.2	1.6	16.1	0.05	-9.5
Autumn (SON)	105.2	-10.9	-1.6	18.6	-0.2	-11.0

Note: Positive values indicate reinforcement, whereas negative values indicate compensation. Contributions may exceed 100% when offset by negative terms

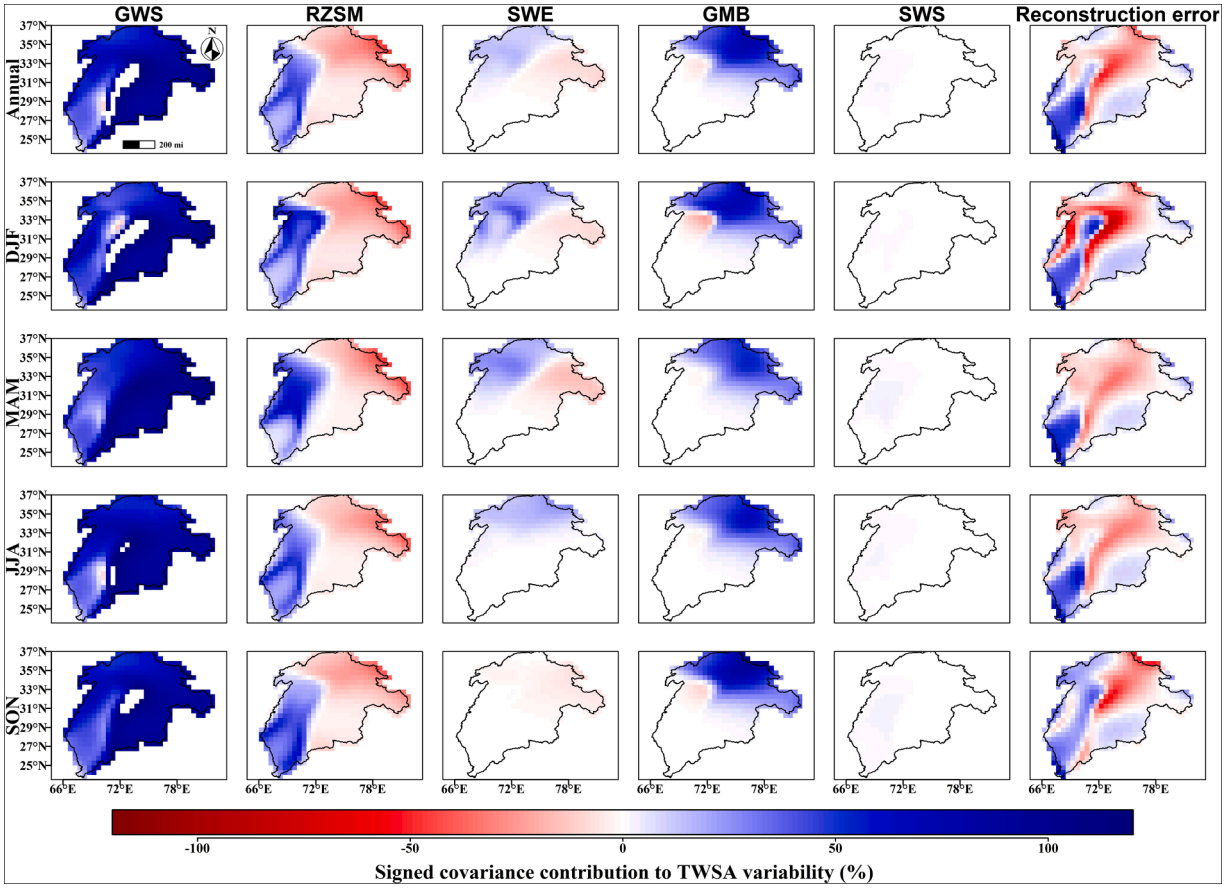


Fig. 5. Annual and seasonal signed covariance contributions of GWS, RZSM, SWE, GMB, SWS, and reconstruction error anomalies to GRACE-derived TWSA variability across the IRB. Positive values reinforce TWSA variability, whereas negative values indicate compensation.

3.4. Basin-scale trends in groundwater storage and drought conditions

The long-term trends in GRACE-derived GWS anomalies and the GRACE-based groundwater drought index (GGDI) were assessed for two periods, 2002–2015 and 2016–2023, across the IRB as shown in Fig. 6. Sen's slope analysis of basin-averaged GWS revealed a slight decline of −0.35 mm/year during 2002–2015, indicating relatively stable groundwater conditions. In contrast, the period 2016–2023 exhibited a substantially higher depletion rate of −13.87 mm/year, suggesting an accelerated drawdown of groundwater resources in recent years, with depletion extending from the semi-arid regions into the more humid parts of the basin (Fig. 6).

The GGDI trends largely mirrored the observed changes in GWS. During 2002–2015, GGDI exhibited a slight statistically significant positive trend (0.023 units yr^{-1}, Kendall's $\tau = 0.208$, $p < 0.001$), indicating overall stable groundwater conditions, although localized drought persisted in arid and semi-arid areas. In contrast, the 2016–2023 period showed a statistically significant negative trend (-0.096 units yr^{-1}, Kendall's $\tau = -0.239$, $p = 0.002$), reflecting both an increase in the severity and frequency of groundwater droughts and an expansion of drought conditions from semi-arid to humid and cold regions. Interestingly, certain arid areas displayed a positive GGDI trend during the latter period, highlighting spatial heterogeneity in groundwater drought responses across the basin (Fig. 6). Collectively, these results suggest that the IRB experienced relatively stable groundwater conditions during 2002–2015, followed by a marked intensification of groundwater depletion and drought risk from 2016 onwards.

3.5. Attribution of GRACE-derived groundwater storage anomalies

The attribution analysis identified distinct contributions associated with climate-related and anthropogenic-associated variables on GRACE-derived GWSA variability across the IRB during 2002–2023 (Fig. 7a). The observed GWSA exhibits a persistent decline that closely follows the anthropogenic-associated component, indicating that long-term groundwater depletion is predominantly linked to human water use. In contrast, the climate-related component exhibits pronounced interannual variability but no sustained long-term decline, suggesting that climatic variability mainly modulates short-term fluctuations rather than driving the long-term storage loss.

Seasonal patterns further clarify the relative roles of these drivers (Fig. 7b). Climate-related GWSA exhibits a clear seasonal cycle, with positive anomalies during the monsoon and late-summer months (June–September) reflecting precipitation-driven recharge, and

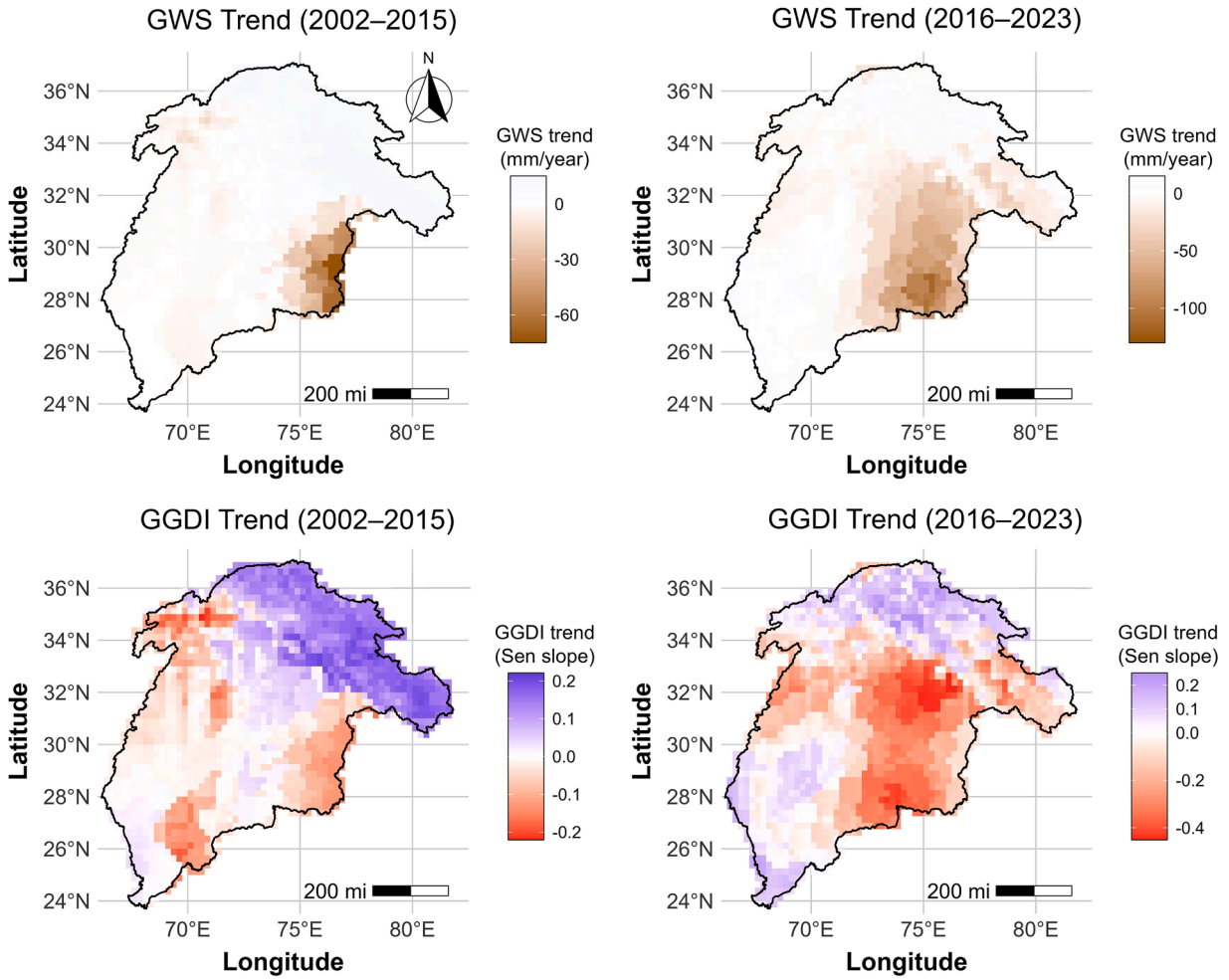


Fig. 6. Spatial distribution of GWS anomalies and GGDI trends across the IRB for 2002–2015 and 2016–2023.

negative anomalies during winter and early spring. In contrast, the anthropogenic-associated component remained predominantly negative throughout the year; however, this should not be interpreted as evidence of uniform groundwater abstraction in every month. Because the long-term trend dominates the total signal, groundwater storage remains below the reference-period mean throughout most of the year. Therefore, the estimated anthropogenic-associated component primarily represents persistent groundwater depletion rather than the complete month-to-month pattern of groundwater pumping. This pattern is consistent with sustained groundwater overexploitation reported in Punjab, Haryana, Rajasthan, and other parts of the IRB, where annual groundwater abstraction exceeds natural recharge (IGRAC, n.d.). The observed monthly GWSA largely follows this anthropogenic-associated signal but shows partial seasonal recovery during the monsoon period due to climate-related recharge. To strengthen the attribution analysis, GRACE-derived GWSA was evaluated against observation-based estimates from 3336 monitoring wells with long-term records spanning 2004–2024 in areas of pronounced groundwater depletion across the IRB (Supplementary Section S7, Fig. S6).

3.6. Basin- and regional-scale separation of climate-related and anthropogenic-associated contributions to GRACE-derived TWSA

Fig. 8 shows contrasting regional patterns in reconstructed TWSA and its attributed components. In the arid and semiarid regions, storage declines broadly follow the anthropogenic-associated component, particularly after 2016, while climate-related fluctuations remain centred near zero. In the cold region, the climate-related component follows much of the seasonal variability and later decline, with a comparatively small anthropogenic-associated signal. Both components become increasingly negative in the humid region. At the basin scale, the sharper decline during the later years, particularly after 2016, coincides with a stronger anthropogenic-associated decrease and a more gradual climate-related decline.

During 2002–2015, the relative magnitude shares of the climate-related and anthropogenic-associated components were 28% and 47% in the arid region and 12% and 59% in the semiarid region, respectively. Climate-related shares exceeded anthropogenic-associated shares in the humid (41% versus 29%) and cold (55% versus 27%) regions. At the basin scale, the corresponding shares

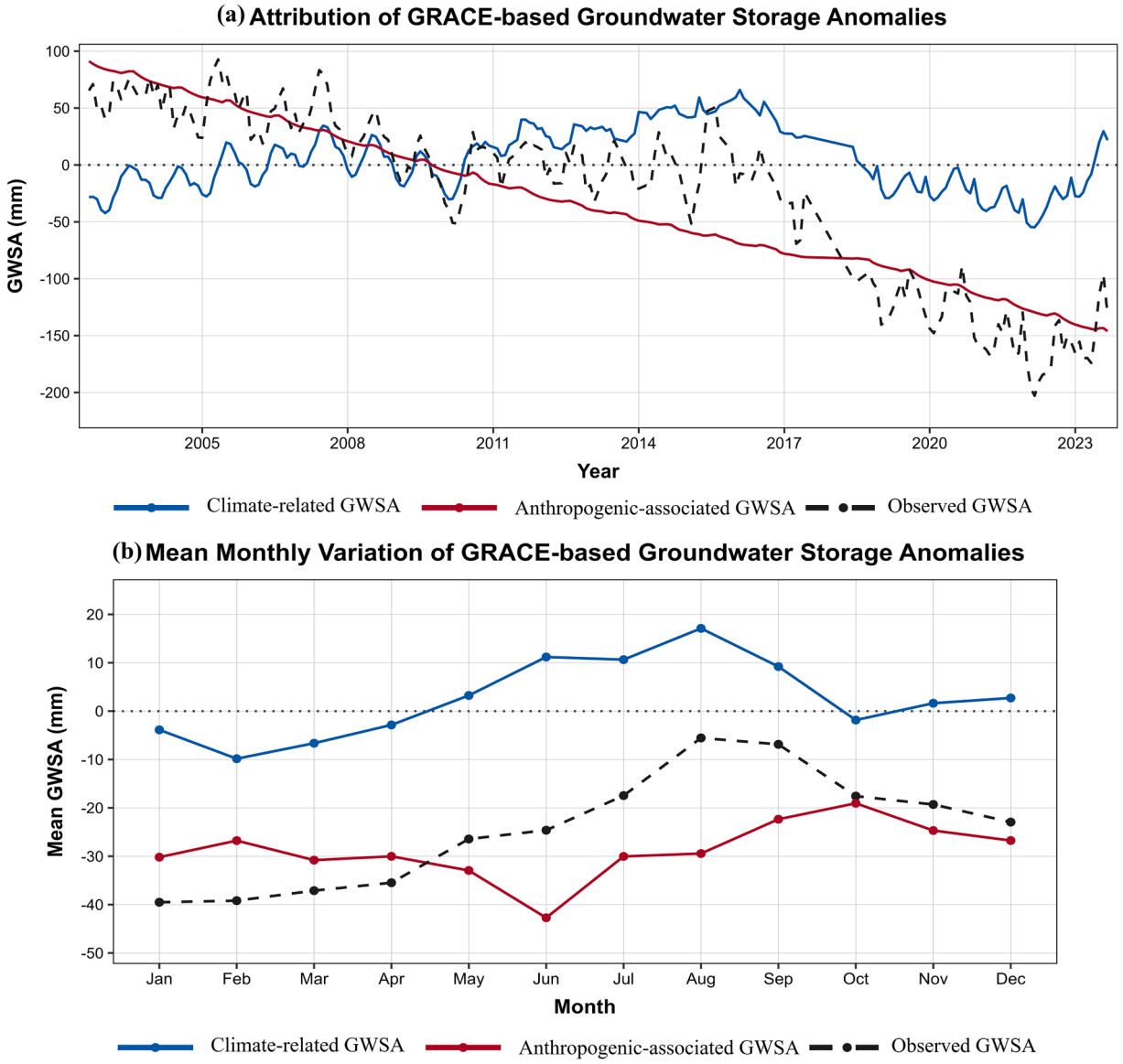


Fig. 7. Attribution of GRACE-derived GWSA in the IRB (2002–2023): (a) GRACE-derived GWSA, climate-driven, and anthropogenic-induced GWSA time series; (b) mean monthly variations showing seasonal groundwater recharge and depletion patterns.

were 33% and 43% (Fig. 9).

During 2016–2023, anthropogenic-associated shares increased to 59% in the arid region and 67% in the semiarid region, while climate-related shares decreased to 24% and 9%, respectively. The humid region showed comparable climate-related and anthropogenic-associated shares (38% and 36%), whereas the cold region retained a larger climate-related share (55% versus 20%). Basin-wide, the anthropogenic-associated share increased to 51%, while the climate-related share declined to 30% (Fig. 9). These percentages represent each component's share of the combined absolute magnitudes of the climate-related, anthropogenic-associated and model residual components; they do not represent fractions of the observed TWSA decline.

The attribution framework showed positive long-term predictive skill across all regions, with out-of-fold R^2 values of 0.36 (arid), 0.72 (semi-arid), 0.71 (humid), 0.33 (cold) and 0.72 (Indus River Basin), and RMSE ranging from 25.3 to 60.0 mm (Table S2). Total-TWSA R^2 ranged from 0.40 to 0.70, although skill at shorter timescales was inconsistent and long-term residuals remained strongly autocorrelated (lag-1 r = 0.98–0.99). Sensitivity tests indicated greater dependence on anthropogenic predictors in the arid and semi-arid zones and on climate predictors in the humid and cold zones; both groups improved basin-scale performance (Table S3). Excluding GWSA reduced long-term R^2 by 0.71 and 1.07 in the arid and semi-arid zones, compared with 0.08, 0.03 and approximately 0.15 in the humid, cold and basin models, respectively. Anthropogenic attribution in the water-limited zones therefore remains conditional on the GRACE-derived GWSA predictors. Full diagnostics are provided in Supplementary Section S8.

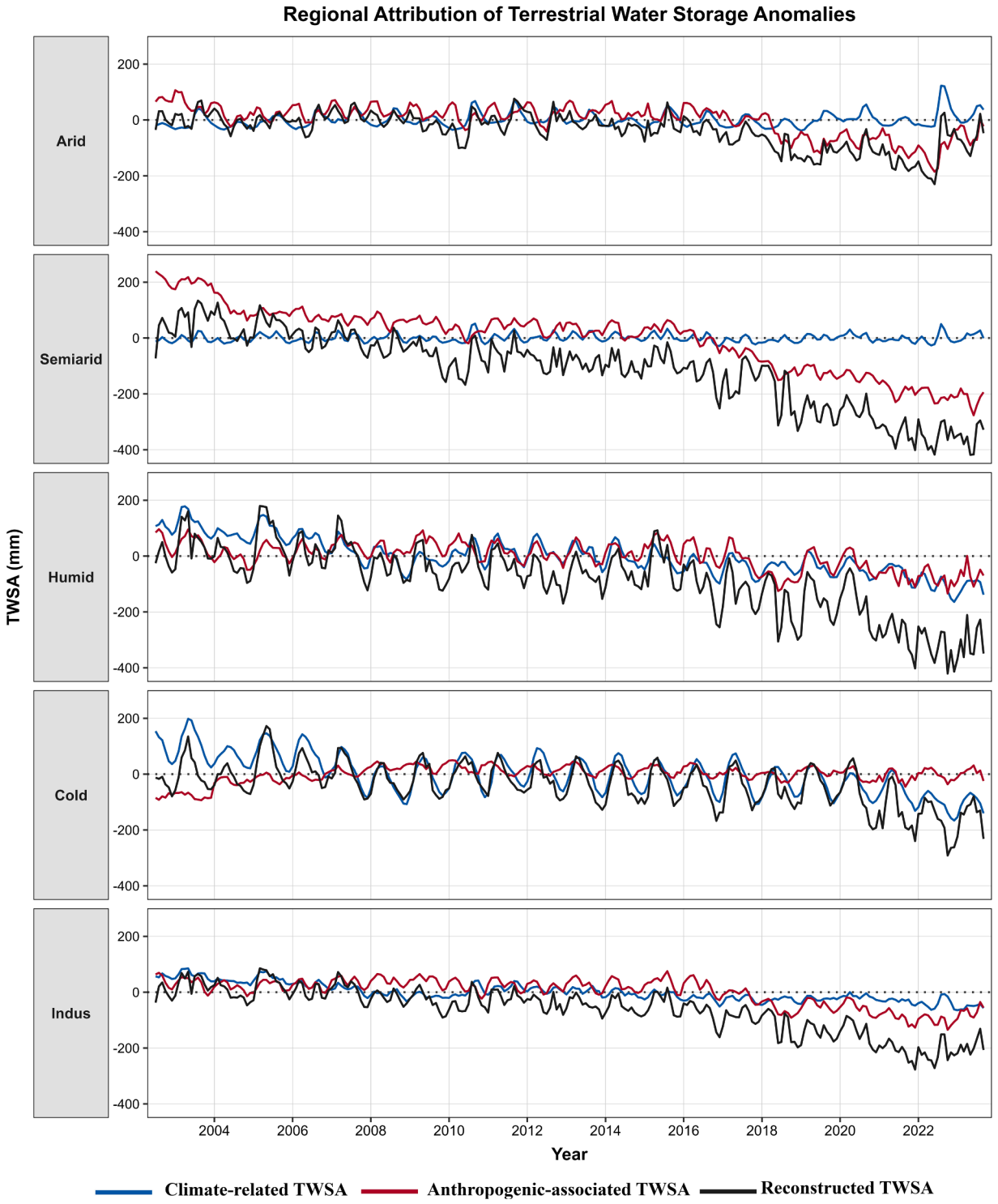


Fig. 8. Regional attribution of GRACE-derived TWSA, showing the separation of observed TWSA into climate-related and anthropogenic-associated components across the arid, semiarid, humid, cold, and entire IRB.

3.7. Spatial trends of GRACE-derived TWSA and its climate-related and anthropogenic-associated components

Fig. 10 presents the broad spatial patterns of ordinary least-squares (OLS) trends in GRACE-derived TWSA and its attributed components across the IRB, displayed on the 0.25° CSR mascon output grid. The reported basin-scale values are area-weighted

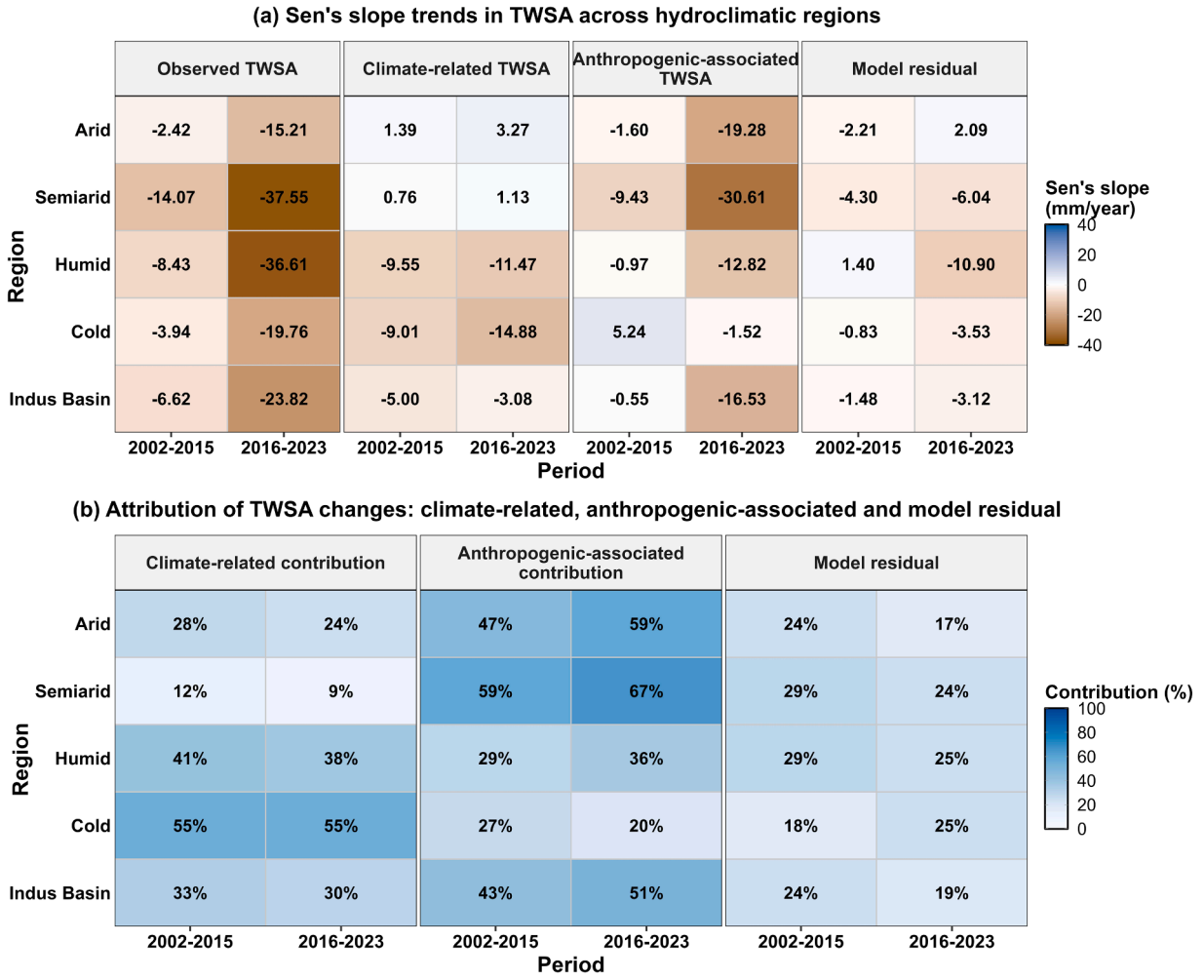


Fig. 9. Regional and basin-wide TWSA attribution during 2002–2015 and 2016–2023: (a) Sen's slopes (mm yr^{-1}) of observed TWSA and attributed components; (b) relative magnitude shares (%) of climate-related, anthropogenic-associated and model residual components. Shares are not fractions of the observed decline; Sen's slopes are not additive.

averages of the pixel-level trends. During 2002–2015, the basin exhibited a moderate decline in TWSA (−6.43 mm yr^{-1}). The climate-related component showed the largest negative basin-average trend (−4.84 mm yr^{-1}), followed by the model residual (−0.87 mm yr^{-1}) and anthropogenic-associated component (−0.72 mm yr^{-1}). Spatially, however, pronounced anthropogenic-associated declines occurred along the southeastern part of the basin, with positive trends in northern areas partly offsetting these losses in the basin average. Climate-related declines were more widespread across the northern basin. Thus, the relatively small basin-average anthropogenic-associated trend masks substantial spatial variation.

In contrast, during 2016–2023, the rate of TWSA decline increased substantially (−23.30 mm yr^{-1}). The anthropogenic-associated component became the largest negative term (−16.21 mm yr^{-1}), with stronger declines extending across the central and southeastern basin. The climate-related component remained negative (−2.98 mm yr^{-1}), although its basin-average decline was weaker than during 2002–2015. The model residual trend also became more negative (−4.12 mm yr^{-1}), indicating a larger decline not accounted for by the fitted climate-related and anthropogenic-associated components. Overall, the results indicate a shift from a larger climate-related negative trend in the earlier period to a predominantly anthropogenic-associated decline after 2015, while retaining substantial spatial heterogeneity. These patterns describe associations within the fitted attribution framework rather than independent causal effects.

4. Discussions

4.1. Global comparison of water depletion magnitudes and drivers

Our results show that the rate of TWSA depletion in the IRB increased from 0.62 cm yr^{-1} during 2002–2015–1.99 cm yr^{-1} during

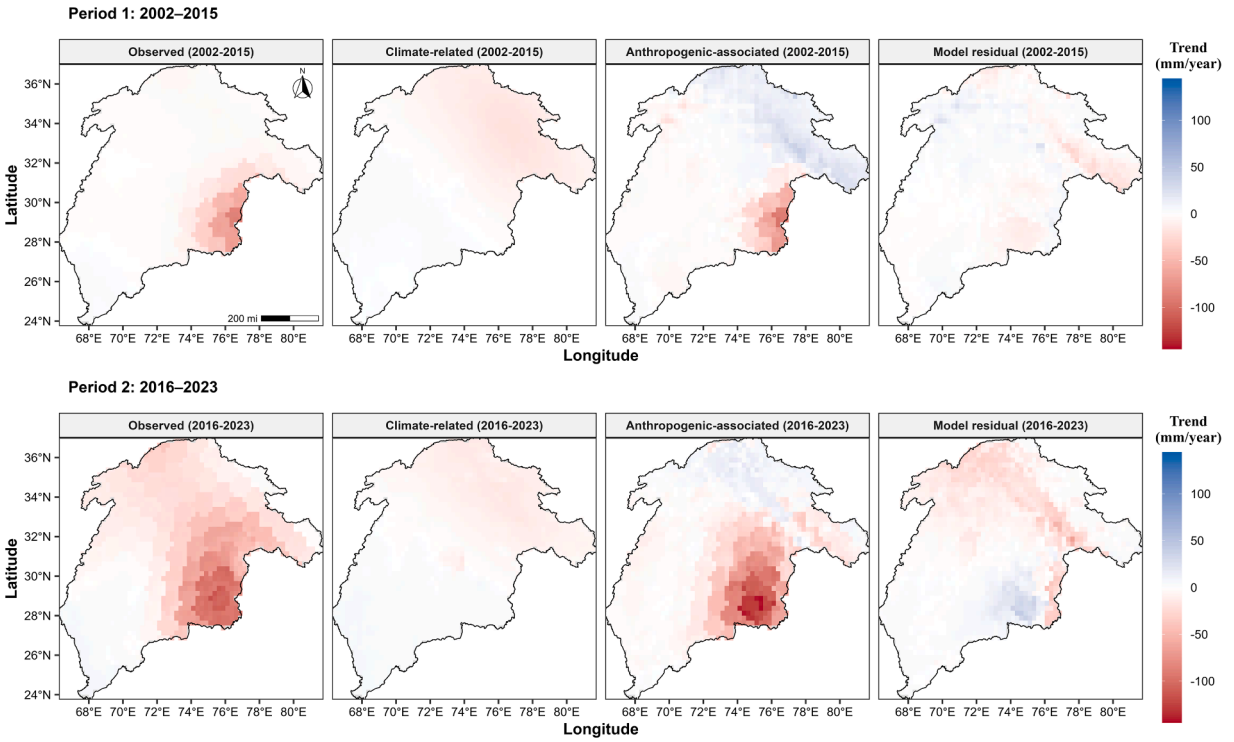


Fig. 10. Spatial distribution of OLS trends (mm yr^{-1}) in observed GRACE-derived TWSA and its climate-related, anthropogenic-associated and model residual components across the IRB during 2002–2015 and 2016–2023. Red and blue indicate negative and positive trends, respectively.

2016–2025, representing more than a threefold increase. During 2016–2023, GWSA declined at a rate of 1.39 cm yr^{-1} . These findings are consistent with an independent GRACE-based assessment, which reported an increase in basin-scale TWSA loss from 0.65 to 2.16 cm yr^{-1} after 2015 and a groundwater-storage decline of 1.44 cm yr^{-1} across the non-glaciated parts of the basin (Dharpure et al., 2025). In both studies, the accelerated depletion is associated with increasing water demand, intensive irrigation, declining precipitation and runoff, higher evapotranspiration, and greater reliance on groundwater during periods of limited surface-water availability.

The groundwater-storage decline observed in the IRB exceeds those reported for Shandong Province and the oasis regions of China (approximately 0.54–0.55 cm yr^{-1} during 2015–2022 and 2002–2023, respectively), but is comparable to declines in Wadi As-Sirhan, northern Saudi Arabia (1.38 cm yr^{-1}), and the Taihang Mountain region of China (2.12 cm yr^{-1} during 2003–2016) (Alshehri and Mohamed, 2023; Liu et al., 2022; Li et al., 2024; Cui et al., 2025). However, it remains lower than the depletion reported for several transboundary aquifers of the Arabian Peninsula (4.63–6.83 cm yr^{-1} during 2010–2021) and California's Central Valley (4.4 $\pm$ 1.4 cm yr^{-1} during 2006–2021) (Argus et al., 2022; Altayyar et al., 2024). Despite differences in magnitude, these regions share similar driving mechanisms, including intensive groundwater abstraction for irrigated agriculture under limited recharge and declining surface-water availability, with drought and long-term aridification further increasing groundwater demand. Comparable processes have also been reported for the Colorado River Basin, where groundwater depletion ranged from 0.12 to 0.33 cm yr^{-1} during 2002–2024 and reached approximately 0.9 $\pm$ 0.1 cm yr^{-1} during the 2004–2013 drought; in the Lower Basin, groundwater depletion accounted for nearly 60% of the total water-storage decline (Castle et al., 2014; Abdelmohsen et al., 2025; Scanlon et al., 2025). These comparisons place the IRB among the major global groundwater-depletion hotspots and indicate that its recent acceleration reflects the combined effects of intensive groundwater use and increasing hydroclimatic stress.

4.2. Drivers of post-2016 water-storage depletion in the IRB

The intensification and geographic spread of groundwater depletion after 2015–2016 likely resulted from the combined effects of increasing irrigation demand, declining reliability of canal-water supplies, increase of groundwater-dependent agriculture and continued cultivation of water-intensive crops across the IRB. Across Punjab and parts of Haryana and Rajasthan within the Indian portion of the IRB, groundwater abstraction has been sustained by low pumping costs, electricity subsidies, and intensive agriculture, with withdrawals commonly exceeding annual recharge and many groundwater assessment units classified as critical or overexploited (Chindarkar and Grafton, 2019; Panda et al., 2021; Central Ground Water Board CGWB, 2023; Central Ground Water Board CGWB, 2025; IGRAC, n.d.). In the Pakistani portion of the IRB, particularly in transboundary areas, rapid expansion of tube wells, limited regulation of groundwater abstraction, population growth, and agricultural intensification have further increased dependence on

groundwater (Hasan and Fatima, 2025). These anthropogenic pressures have interacted with monsoon variability, shifts in snowmelt timing, rising temperatures, and increasing crop-water demand, resulting in greater groundwater abstraction during periods of reduced rainfall and limited surface-water availability (Asoka et al., 2017; Dangar et al., 2021). The expansion of agricultural and urban areas may have further intensified groundwater demand while limiting recharge, thereby extending depletion across the intensively cultivated lowlands (Cao and Roy, 2025). These processes align with recent GRACE-based studies documenting an increased rate of groundwater depletion and stronger anthropogenic influence after 2015–2016, particularly across the lower Indus plains (Arshad et al., 2024; Dharpure et al., 2025), with potential consequences including salinization, land subsidence, and reduced long-term water security (United Nations University Institute for Water, Environment and Health UNU-INWEH, 2026). The spatial distribution of GWSA is not expected to mirror population density, as groundwater depletion is governed more directly by irrigation intensity, abstraction rates, canal-water availability, recharge conditions, and aquifer properties. Accordingly, GWSA was interpreted as anthropogenic-associated only where its spatial and temporal patterns were supported by independent evidence of intensive groundwater use and irrigated agriculture.

4.3. Methodological considerations and key findings of the decomposition–attribution analysis

Attribution of GRACE-derived TWSA remains challenging due to uncertainties in separating climatic and anthropogenic signals. The applied framework, integrating STL decomposition with lagged elastic net regression and blocked cross-validation, improves attribution robustness by accounting for multicollinearity, temporal dependence, and delayed hydrological responses. By decomposing TWSA prior to attribution, the approach reduces signal mixing and enhances physical interpretability, representing an advance over correlation-based methods (Arshad et al., 2024; Dharpure et al., 2025). The attribution results reveal strong spatial heterogeneity in controls on TWSA across the IRB. In arid and semiarid regions, persistent declines are primarily associated with anthropogenic-associated pressures, indicating that groundwater abstraction and irrigation dominate long-term depletion (Zhu et al., 2021; Mehmood et al., 2022; Arshad et al., 2024; Dharpure et al., 2025). In contrast, variability in humid and cold upstream regions is largely climate-related, reflecting the influence of precipitation variability and snow processes (Zhu et al., 2021; Arshad et al., 2024). The intensified depletion after the mid-2010s suggests a combined effect of increasing anthropogenic-associated water use in downstream semiarid regions and enhanced climate-related variability in upstream areas.

4.4. Limitations and uncertainties

Uncertainties in this assessment arise from both observational datasets and the attribution methodology. The GRACE CSR Mascon product (RL06; Save et al., 2016, Save, 2020) substantially reduces signal leakage and attenuation errors relative to earlier solutions (Landerer and Swenson, 2012; Wiese et al., 2016) and incorporates mascon corrections to minimize leakage from adjacent regions (Ditmar, 2018). The applied GIA correction further improves long-term TWSA estimates. However, some limitations remain. For example, the 0.25° spatial resolution of the CSR mascon product represents the output grid spacing rather than the actual effective resolution of GRACE on which the solution is distributed and does not reflect the actual, much coarser spatial resolution of GRACE observations. Accordingly, the mapped TWSA trends and component contributions are interpreted at the basin and hydroclimatic-zone scales, rather than as independent estimates for individual 0.25° grid cells. This consideration is especially important in the IRB, where groundwater abstraction, irrigation, surface-water storage, and cryospheric processes can vary over short distances. However, recent studies integrated GRACE with independent geodetic observations, for instance, Zhu et al. (2025) showed that jointly inverting GNSS and InSAR observations provides additional constraints for estimating regional TWSA variations, whereas, Wang et al., (2026) demonstrated that integrating GNSS and GRACE observations can improve the assessment of spatially heterogeneous TWS changes and the evolution of hydrological drought. Therefore, the integration of independent geodetic observations should be prioritized in future studies to improve the assessment of TWSA changes across the IRB.

Nevertheless, GravIS and G3P component datasets inherit GRACE-related uncertainties and additional errors associated with the separation of individual storage components (Dahle et al., 2025; Pasik et al., 2023). Additional uncertainty arises from the mismatch between point-based groundwater observations and the coarse spatial resolution of GRACE, which limits the representation of localized variability and contributes to discrepancies in validation results. Another source of uncertainty is the use of a single uniform specific-yield value across the study area because spatially distributed specific-yield data are unavailable for the IRB. Consequently, part of the amplitude mismatch between the well-based and GRACE-derived GWSA estimates may result from this assumption, together with differences in spatial scale, aquifer depth, confinement, pumping, and recharge conditions.

Attribution uncertainty is also introduced by the selection of predictor variables, their classification into climatic and anthropogenic groups, and the use of lagged relationships, which may influence the partitioning of TWSA components. Although the framework quantifies the relative influence of climate-related and anthropogenic-related processes, these groups are not fully independent because several hydrological variables are affected by both natural variability and water management. Therefore, the results represent model-based contributions rather than exclusive causal effects. A limitation of the framework is that the seasonal–interannual component was treated as predominantly climate-related. Although these timescales are largely controlled by hydroclimatic processes, irrigation and reservoir operations may also contribute, causing some anthropogenic-associated variability to be included in the estimated climate-related signal.

Uncertainty may arise because basin averaging, temporal decomposition and elastic-net regularization can suppress seasonal pumping signals, while irrigation-related variability that covaries with precipitation, evaporation, or recharge may be partly assigned to the climate component. Furthermore, partial dependence among storage components, particularly the inclusion of GWS within total

TWSA, may introduce residual overlap in attribution signals. Uncertainty in GLDAS CLSM (Rodell et al., 2004) arises from the underrepresentation of irrigation, soil moisture dynamics, and evaporation in intensively irrigated regions. The limited representation of irrigation processes in GLDAS-CLSM in heavily irrigated regions may influence the simulated TWSA components, allowing part of the irrigation signal to remain in the residual GWS estimate. As a result, the magnitude and spatial distribution of the derived groundwater anomalies may be affected. Another limitation of GLDAS-CLSM data is the partial dependence between GRACE and GLDAS-CLSM v2.2 due to GRACE-based data assimilation, which may introduce some inherited GRACE information into the residual groundwater estimates. Since GRACE TWSA was not used as a predictor, direct mathematical circularity was avoided.

The ERA5-based datasets exhibit biases in SWE and snow processes in complex terrain (Muñoz-Sabater et al., 2021; Kouki et al., 2023). Despite these limitations, the integration of multiple independent datasets and a physically informed statistical framework supports a consistent and robust assessment of TWSA variability across the IRB.

5. Conclusions

This study quantified GRACE-derived TWSA dynamics across the IRB using an extended record spanning April 2002 to August 2025. By separating periods before and after the shift around 2015 and stratifying the basin into arid, semiarid, humid, and cold zones, the analysis resolved major temporal and spatial differences in water storage change that are not evident from basin-mean assessments.

GRACE-derived TWSA reveals accelerated and spatially expanding depletion across the IRB. During 2002–2015, the strongest decline occurred in the semiarid region (-16.1 mm yr^{-1}), followed by the humid (-6.85 mm yr^{-1}), cold (-3.65 mm yr^{-1}), and arid (-1.95 mm yr^{-1}) regions. After 2016, depletion intensified substantially, reaching -34.96 mm yr^{-1} in the semiarid, -39.80 mm yr^{-1} in the humid, and -27.35 mm yr^{-1} in the cold regions, whereas the arid region showed modest recovery after 2021. At the basin scale, mean TWSA declined from -13.7 mm (2002–2015) to -168.6 mm (2016–2025), and Sen's slope strengthened from -6.5 to -22.5 mm yr^{-1} , indicating a marked intensification of basin-wide storage loss.

Covariance decomposition showed that GWSA was the dominant model-derived component associated with TWSA variability, contributing 103.9% annually and 99.9–105.2% seasonally. Values above 100% were offset by negative contributions from other components and the reconstruction error. GMB made a moderate contribution, whereas RZSM acted mainly as a compensating term and SWE and SWSA were minor. Spatial patterns broadly supported the basin-scale results, with widespread positive GWSA contributions, regionally contrasting RZSM effects, and SWE and GMB contributions concentrated in the upper cryospheric region. SWS anomalies remained minor.

Basin-scale groundwater conditions were relatively stable during 2002–2015, with GWS anomalies declining only slightly (-0.35 mm yr^{-1}) and GGDI showing a weak positive trend (0.023). In contrast, 2016–2023 was characterized by a sharp intensification of groundwater depletion, with GWS declining at -13.87 mm yr^{-1} and GGDI decreasing to -0.096, indicating increasing severity and spatial expansion of groundwater drought across the IRB.

During 2016–2023, anthropogenic-associated components had the largest relative magnitude shares in arid (59%) and semiarid (67%) regions, whereas the climate-related share was largest in the cold region (55%). Shares were comparable in the humid region (38% climate-related; 36% anthropogenic-associated). Basin-wide, observed TWSA declined at -23.82 mm yr^{-1} ; anthropogenic-associated, climate-related and residual Sen's slopes were -16.53, -3.08 and -3.12 mm yr^{-1} , with magnitude shares of 51%, 30% and 19%, respectively. These shares are not fractions of the observed decline, and Sen's slopes are not additive.

Overall, the IRB is undergoing accelerated and spatially heterogeneous water storage decline, with anthropogenic-associated pressure dominating in arid and semiarid regions and climate-related processes exerting stronger influence in humid and cold regions. These findings highlight the need for region-specific management, particularly to reduce unsustainable groundwater abstraction in downstream semiarid areas and to strengthen adaptation to increasing climatic stress in upstream cryosphere-influenced regions.

CRediT authorship contribution statement

Muhammad Adnan: Writing – original draft, Visualization, Validation, Software, Resources, Methodology, Formal analysis, Data curation, Conceptualization. **Leilei Yong:** Writing – review & editing, Methodology, Data curation. **Qiaojuan Xi:** Writing – review & editing, Resources. **Muhammad Saifullah:** Writing – review & editing, Resources, Data curation. **Qaisar Saddique:** Writing – review & editing, Resources, Data curation. **Waqas Ul Hussan:** Writing – review & editing, Resources, Data curation. **Hongkai Gao:** Writing – review & editing, Supervision, Funding acquisition.

Funding

The current study is supported by the National Natural Science Foundation of China (grant no. 42471040), and the National Key Research and Development Program of China (grant nos. 2024YFE0113200 and 2024YFF0809304).

Declaration of Competing Interest

The authors declare that they have no known competing financial interests or personal relationships that could have appeared to influence the work reported in this paper.

Acknowledgement

The authors thank the Center for Space Research (CSR) at The University of Texas at Austin for making the GRACE and GRACE-FO Mascon TWSA data (Release RL06.3) publicly accessible. We also appreciate NASA's Goddard Earth Sciences Data and Information Services Center (GES DISC) for providing the GLDAS Catchment Land Surface Model (CLSM) version 2.2 dataset. Groundwater and other terrestrial water storage component data were obtained from the Gravity Information Service (GravIS) operated by the GFZ German Research Centre for Geosciences, and we sincerely acknowledge GFZ for making these datasets openly available. The authors acknowledge the International Groundwater Resources Assessment Centre (IGRAC) for providing open-access groundwater data through its Global Groundwater Information System (GGIS) and Global Groundwater Monitoring Network (GGMN). We also acknowledge the contributions of national agencies, particularly the Central Ground Water Board (CGWB), India, for groundwater monitoring data made available through IGRAC. We thank the WaterGAP and MIRCA-OS development teams for making the irrigation-withdrawal and irrigated-area datasets publicly available.

Appendix A. Supporting information

Supplementary data associated with this article can be found in the online version at doi:10.1016/j.ejrh.2026.104117.

Data availability

Data will be made available on request.

References

Abdelmohsen, K., Famiglietti, J.S., Ao, Y.Z., Mohajer, B., Chandanpurkar, H.A., 2025. Declining freshwater availability in the Colorado River Basin threatens sustainability of its critical groundwater supplies. Geophys. Res. Lett. 52, e2025GL115593. https://doi.org/10.1029/2025GL115593.

Abdullah, T., Romshoo, S.A., Rashid, I., 2020. The satellite-observed glacier mass changes over the Upper Indus Basin during 2000–2012. Sci. Rep. 10, 14285. https://doi.org/10.1038/s41598-020-71281-7.

Akhtar, F., Nawaz, R.A., Hafeez, M., Awan, U.K., Borgemeister, C., Tischbein, B., 2022. Evaluation of GRACE-derived groundwater storage changes in different agro-ecological zones of the Indus Basin. J. Hydrol. 605, 127369. https://doi.org/10.1016/j.jhydrol.2021.127369.

Akl, M., Thomas, B.F., Clarke, P.J., 2025. Global groundwater drought assessment revisited: A holistic re-evaluation of the GRACE-groundwater drought index across major aquifers. Water Resour. Res. 61, e2025WR040389. https://doi.org/10.1029/2025WR040389.

Ali, S., Cheema, M.J.M., Waqas, M.M., Waseem, M., Awan, U.K., Khaliq, T., 2020. Changes in snow cover dynamics over the Indus Basin: evidences from 2008 to 2018 MODIS NDSI trends analysis. Remote. Sens. 12, 2782. https://doi.org/10.3390/rs12172782.

Ali, S., Wang, Q., Liu, D., Fu, Q., Rahaman, M.M., Faiz, M.A., Cheema, M.J.M., 2022. Estimation of spatio-temporal groundwater storage variations in the Lower Transboundary Indus Basin using GRACE satellite. J. Hydrol. 605, 127315. https://doi.org/10.1016/j.jhydrol.2021.127315.

Alshehri, F., Mohamed, A., 2023. Analysis of groundwater storage fluctuations using GRACE and remote sensing data in Wadi As-Sirhan, northern Saudi Arabia. Water 15, 282. https://doi.org/10.3390/w15020282.

Altayyar, M.O., Ali, S., Larson, A.E., Boving, T., Thiem, L., Akanda, A.S., 2024. Quantifying groundwater depletion in Arabian Peninsula transboundary aquifer systems: Understanding natural and anthropogenic drivers. Groundw. Sustain. Dev. 26, 101293. https://doi.org/10.1016/j.gsd.2024.101293.

Argus, D.F., Martens, H.R., Borsa, A.A., Knappe, E., Wiese, D.N., Alam, S., Anderson, M., Khatiwada, A., Laus, N., Peidou, A., Swar, M., White, A.M., Bo, M.S., Ellmer, M., Landerer, F.W., Gardiner, W.P., 2022. Subsurface water flux in California's Central Valley and its source watershed from space geodesy. Geophys. Res. Lett. 49, e2022GL099583. https://doi.org/10.1029/2022GL099583.

Arshad, A., Mirchi, A., Taghvaeian, S., AghaKouchak, A., 2024. Downscaled-GRACE data reveal anthropogenic and climate-induced water storage decline across the Indus Basin. Water Resour. Res. 60, e2023WR035882. https://doi.org/10.1029/2023WR035882.

Asoka, A., Gleeson, T., Wada, Y., Mishra, V., 2017. Relative contribution of monsoon precipitation and pumping to changes in groundwater storage in India. Nat. Geosci. 10, 109–117. https://doi.org/10.1038/ngeo2869.

Bhanja, S.N., Mukherjee, A., Saha, D., Velicogna, I., Famiglietti, J.S., 2016. Validation of GRACE-based groundwater storage anomaly using in situ groundwater-level measurements in India. J. Hydrol. 543, 729–738. https://doi.org/10.1016/j.jhydrol.2016.10.042.

Bocchiola, D., Soncini, A., 2019. Water resources modeling and prospective evaluation in the Indus River under present and prospective climate change. Indus River Basin. Elsevier, pp. 17–56. https://doi.org/10.1016/B978-0-12-812782-7.00002-3.

Cao, Y., Ge, G., Bao, Y., Chang, A., Niu, R., 2025. Study on the changing trend of terrestrial water storage in Inner Mongolia based on GRACE satellite and GLDAS hydrological model. Water 17, 3123. https://doi.org/10.3390/w17213123.

Cao, Y., Roy, S.S., 2025. Groundwater depletion in India: The influence of seasonal precipitation and land use land cover. Environ. Sci. Pollut. Res. 32, 30833–30845. https://doi.org/10.1007/s11356-025-37274-7.

Castle, S.L., Thomas, B.F., Reager, J.T., Rodell, M., Swenson, S.C., Famiglietti, J.S., 2014. Groundwater depletion during drought threatens future water security of the Colorado River Basin. Geophys. Res. Lett. 41, 5904–5911. https://doi.org/10.1002/2014GL061055.

Center for Space Research (CSR), University of Texas at Austin, 2025. GRACE RL06 Mascon Solutions. https://www2.csr.utexas.edu/grace/RL06_mascons.html (accessed 10 July 2026).

Central Ground Water Board, 2013. Ground Water Year Book—India (2012–2013). Ministry of Water Resources, Government of India, New Delhi.

Central Ground Water Board, 2017. Aquifer Systems of India. Ministry of Water Resources, Government of India, New Delhi.

Central Ground Water Board (CGWB), 2023. Dynamic Ground Water Resources of India, 2023. Department of Water Resources, River Development and Ganga Rejuvenation, Ministry of Jal Shakti, Government of India.

Central Ground Water Board (CGWB), 2025. National Compilation on Dynamic Ground Water Resources of India, 2025. Department of Water Resources, River Development and Ganga Rejuvenation, Ministry of Jal Shakti, Government of India.

Chao, N., Li, F., Yu, N., Chen, G., Wang, Z., Ouyang, G., Yeh, P.J.-F., 2023. Divergent spatiotemporal variability of terrestrial water storage and eight hydroclimatic components over three different scales of the Yangtze River basin. Sci. Total. Environ. 879, 162886. https://doi.org/10.1016/j.scitotenv.2023.162886.

Cheema, M.J.M., Immerzeel, W.W., Bastiaanssen, W.G.M., 2014. Spatial quantification of groundwater abstraction in the irrigated Indus Basin. Groundwater 52, 25–36. https://doi.org/10.1111/gwat.12027.

Chen, J., Famiglietti, J.S., Scanlon, B.R., Rodell, M., 2016. Groundwater storage changes: Present status from GRACE observations. In: Baghdadi, N., Zribi, M. (Eds.), Remote Sensing and Water Resources. Springer International Publishing, Cham, pp. 207–227. https://doi.org/10.1007/s10712-015-9332-4.
Chindarkar, N., Grafton, R.Q., 2019. India's depleting groundwater: When science meets policy. Asia Pac. Policy Stud. 6, 108–124. https://doi.org/10.1002/app5.269.
Cleveland, R.B., Cleveland, W.S., McRae, J.E., Terpenning, I., 1990. STL: A seasonal-trend decomposition procedure based on Loess. J. Off. Stat. 6, 3–73.
Copernicus Climate Change Service (C3S), 2025. ERA5-Land hourly data from 1950 to present. https://cds.climate.copernicus.eu/datasets/reanalysis-era5-land (accessed 10 July 2026).
Cui, B., Xue, D., Gui, D., Liu, Q., Abd-Elmabod, S.K., Chen, X., De Maeyer, P., 2025. Downscaled GRACE data reveal anthropogenic dominance in groundwater storage decline across China's oases. Ecol. Indic. 179, 114209. https://doi.org/10.1016/j.ecolind.2025.114209.
Dahle, C., Boergens, E., Sasgen, I., Döhne, T., Reißland, S., Dobslaw, H., Klemann, V., Murböck, M., König, R., Dill, R., Sips, M., Sylla, U., Groh, A., Horwath, M., Flechtner, F., 2025. GravIS: mass anomaly products from satellite gravimetry. Earth Syst. Sci. Data 17, 611–631. https://doi.org/10.5194/essd-17-611-2025.
Dangar, S., Asoka, A., Mishra, V., 2021. Causes and implications of groundwater depletion in India: A review. J. Hydrol. 596, 126103. https://doi.org/10.1016/j.jhydrol.2021.126103.
Dars, G.H., Najafi, M.R., Qureshi, A.L., 2017. Assessing the impacts of climate change on future precipitation trends based on downscaled CMIP5 simulation data. Mehran Univ. Res. J. Eng. Technol. 36, 385–394. https://doi.org/10.22581/muet1982.1702.16.
Davidson, N.C., 2018. Indus waters treaty. In: Finlayson, C.M., Milton, G.R., Prentice, R.C., Davidson, N.C. (Eds.), The Wetland Book. Springer, Dordrecht, pp. 4–5. https://doi.org/10.1007/978-94-007-6172-8_132-1.
Dharpure, J.K., Howat, I.M., Kaushik, S., 2025. Declining groundwater storage in the Indus Basin revealed using GRACE and GRACE-FO data. Water Resour. Res. 61, e2024WR038279. https://doi.org/10.1029/2024WR038279.
Ditmar, P., 2018. Conversion of time-varying Stokes coefficients into mass anomalies at the Earth's surface considering the Earth's oblateness. J. Geod. 92, 1401–1412. https://doi.org/10.1007/s00190-018-1128-0.
Eicker, A., Forootan, E., Springer, A., Longuevergne, L., Kusche, J., 2016. Does GRACE see the terrestrial water cycle "intensifying"? J. Geophys. Res. Atmos. 121, 733–745. https://doi.org/10.1002/2015JD023808.
Food and Agriculture Organization of the United Nations (FAO), 2011. AQUASTAT Transboundary River Basins—Ganges–Brahmaputra–Meghna River Basin. https://www.fao.org/aquastat/ (accessed 10 July 2026).
Feng, S., Liu, J., Zhang, Q., Zhang, Y., Singh, V.P., Gu, X., Sun, P., 2020. A global quantitation of factors affecting evapotranspiration variability. J. Hydrol. 584, 124688. https://doi.org/10.1016/j.jhydrol.2020.124688.
Getirana, A., Kumar, S., Rodell, M., 2025. Inconsistencies in GRACE-based groundwater storage estimation—a call for a proper use of land surface models. Geophys. Res. Lett. 52, e2025GL119197. https://doi.org/10.1029/2025GL119197.
Girotto, M., Rodell, M., 2019. Terrestrial water storage. Extreme Hydroclimatic Events and Multivariate Hazards in a Changing Environment. Elsevier, ISBN 9780128148990, pp. 41–64. https://doi.org/10.1016/b978-0-12-814899-0.00002-x. https://linkinghub.elsevier.com/retrieve/pii/B978012814899000002X.
Gruber, S., 2012. Derivation and analysis of a high-resolution estimate of global permafrost zonation. Cryosphere 6, 221–233. https://doi.org/10.5194/tc-6-221-2012.
Güntner, A., Sharifi, E., Haas, J., Boergens, E., Dahle, C., Dobslaw, H., Dorigo, W., Dussailant, I., Flechtner, F., Jäggi, A., Kosmale, M., Luojus, K., Mayer-Gürr, T., Meyer, U., Preimesberger, W., Ruz Vargas, C., Zemp, M., 2024. Global Gravity-based Groundwater Product (G3P). GFZ Data Serv. V1.12. https://doi.org/10.5880/G3P.2023.001.
Haddeland, I., Heinke, J., Biemans, H., Eisner, S., Flörke, M., Hanasaki, N., Wada, Y., Wisser, D., 2014. Global water resources affected by human interventions and climate change. Proc. Natl. Acad. Sci. U. S. A. 111, 3251–3256. https://doi.org/10.1073/pnas.1222475110.
Hasan, F.U., Fatima, B., 2025. A review of drivers contributing to unsustainable groundwater consumption in Pakistan. Groundw. Sustain. Dev. 29, 101414. https://doi.org/10.1016/j.gsd.2025.101414.
Huang, J., Li, Y., Fu, C., Chen, F., Dai, A., Ma, Z., Wang, G., 2017. Dryland climate change: Recent progress and challenges. Rev. Geophys. 55, 719–778. https://doi.org/10.1002/2016RG000550.
Humphrey, V., Gudmundsson, L., Seneviratne, S.I., 2016. Assessing global water storage variability from GRACE: Trends, seasonal cycle, subseasonal anomalies and extremes. Surv. Geophys. 37, 357–395. https://doi.org/10.1007/s10712-016-9367-1.
Humphrey, V., Gudmundsson, L., Seneviratne, S.I., 2017. A global reconstruction of climate-driven subdecadal water storage variability. Geophys. Res. Lett. 44, 2300–2309. https://doi.org/10.1002/2017GL072564.
International Groundwater Resources Assessment Centre (IGRAC), n.d. Groundwater Country Profile: India.
Immerzeel, W.W., van Beek, L.P.H., Bierkens, M.F.P., 2010. Climate change will affect the Asian water towers. Science 328, 1382–1385. https://doi.org/10.1126/science.1183188.
IPCC, 2022. High Mountain Areas. In: Pörtner, H.-O., Roberts, D.C., Tignor, M., Poloczanska, E.S., Mintenbeck, K., Alegría, A., Craig, M., Langsdorf, S., Löschke, S., Möller, V., Okem, A., Rama, B. (Eds.), The Ocean and Cryosphere in a Changing Climate. Cambridge University Press, Cambridge, pp. 131–202. https://doi.org/10.1017/9781009157964.004.
Iqbal, N., Hossain, F., Lee, H., Akhter, G., 2016. Satellite gravimetric estimation of groundwater storage variations over Indus Basin in Pakistan. IEEE J. Sel. Top. Appl. Earth Obs. Remote. Sens. 9, 3524–3534. https://doi.org/10.1109/JSTARS.2016.2574378.
Kebede, E.A., Oluoch, K.O., Siebert, S., Mehta, P., Hartman, S., Jägermeyr, J., Ray, D., Ali, T., Brauman, K.A., Deng, Q., Xie, W., Davis, K.F., 2025. A global open-source dataset of monthly irrigated and rainfed cropped areas (MIRCA-OS) for the 21st century. Sci. Data 12, 208. https://doi.org/10.1038/s41597-024-04313-w.
Kendall, M.G., 1957. Rank Correlation Methods. Griffin, London.
Kouki, K., Luojus, K., Riihelä, A., 2023. Evaluation of snow cover properties in ERA5 and ERA5-Land with several satellite-based datasets in the Northern Hemisphere in spring 1982–2018. Cryosphere 17, 5007–5026. https://doi.org/10.5194/tc-17-5007-2023.
Laghari, A.N., Vanham, D., Rauch, W., 2012. The Indus Basin in the framework of current and future water resources management. Hydrol. Earth Syst. Sci. 16, 1063–1083. https://doi.org/10.5194/hess-16-1063-2012.
Landerer, F.W., Swenson, S.C., 2012. Accuracy of scaled GRACE terrestrial water storage estimates. Water Resour. Res. 48, W04531. https://doi.org/10.1029/2011WR011453.
Lee, H., Jung, M., Carvalhais, N., Trautmann, T., Kraft, B., Reichstein, M., Forkel, M., Koirala, S., 2023. Diagnosing modeling errors in global terrestrial water storage interannual variability. Hydrol. Earth Syst. Sci. 27, 1531–1563. https://doi.org/10.5194/hess-27-1531-2023.
Li, W., Bao, L., Yao, G., Wang, F., Guo, Q., Zhu, J., Zhu, J., Wang, Z., Bi, J., Zhu, C., Zhong, Y., Lu, S., 2024. The analysis on groundwater storage variations from GRACE/GRACE-FO in recent 20 years driven by influencing factors and prediction in Shandong Province, China. Sci. Rep. 14, 5819. https://doi.org/10.1038/s41598-024-55588-3.
Liu, M., Pei, H., Shen, Y., 2022. Evaluating dynamics of GRACE groundwater and its drought potential in Taihang Mountain Region, China. J. Hydrol. 612, 128156. https://doi.org/10.1016/j.jhydrol.2022.128156.
Loomis, B.D., Richey, A.S., Arendt, A.A., Appana, R., Deweese, Y.-J.C., Forman, B.A., Kumar, S.V., Sabaka, T.J., Shean, D.E., 2019. Water storage trends in High Mountain Asia. Front. Earth Sci. 7, 235. https://doi.org/10.3389/feart.2019.00235.
Lopez, T., Al Bitar, A., Biancamaria, S., Güntner, A., Jäggi, A., 2020. On the use of satellite remote sensing to detect floods and droughts at large scales. Surv. Geophys. 41, 1461–1487. https://doi.org/10.1007/s10712-020-09618-0.
Luojus, K., Pulliainen, J., Takala, M., Lemmetyinen, J., Mortimer, C., Derksen, C., Mudryk, L., Moisander, M., Hiltunen, M., Smolander, T., Ikonen, J., Cohen, J., Salminen, M., Norberg, J., Veijola, K., Venäläinen, P., 2021. GlobSnow v3.0 Northern Hemisphere snow water equivalent dataset. Sci. Data 8, 163. https://doi.org/10.1038/s41597-021-00939-2.
Luthcke, S.B., Sabaka, T.J., Loomis, B.D., Arendt, A.A., McCarthy, J.J., Camp, J., 2013. Antarctica, Greenland and Gulf of Alaska land-ice evolution from an iterated GRACE global mascon solution. J. Glaciol. 59, 613–631. https://doi.org/10.3189/2013JoG12J147.

Lutz, A.F., Immerzeel, W.W., Kraaijenbrink, P.D.A., Shrestha, A.B., Bierkens, M.F.P., 2016. Climate change impacts on the upper Indus hydrology: Sources, shifts and extremes. PLoS. One 11, e0165630. https://doi.org/10.1371/journal.pone.0165630.
Lytton, L., Ali, A., Garthwaite, B., Punthakey, J.F., Saeed, B., 2021. Groundwater in Pakistan's Indus Basin: Present and Future Prospects. World Bank, Washington, DC. https://doi.org/10.1596/35065.
MacDonald, A.M., Bonsor, H.C., Ahmed, K.M., Burgess, W.G., Basharat, M., Calow, R.C., Yadav, S.K., 2016. Groundwater quality and depletion in the Indo-Gangetic Basin mapped from in situ observations. Nat. Geosci. 9, 762–766. https://doi.org/10.1038/ngeo2791.
Maina, F.Z., Xue, Y., Kumar, S.V., Getirana, A., McLarty, S., Appana, R., Forman, B., Zaitchik, B., Loomis, B., Maggioni, V., Zhou, Y., 2024. Development of a multidecadal land reanalysis over High Mountain Asia. Sci. Data 11, 827. https://doi.org/10.1038/s41597-024-03643-z.
Mann, H.B., 1945. Nonparametric tests against trend. Econometrica 13, 245–259. https://doi.org/10.2307/1907187.
Mehmood, K., Tischbein, B., Flörke, M., Usman, M., 2022. Spatiotemporal analysis of groundwater storage changes, controlling factors, and management options over the transboundary Indus Basin. Water 14, 3254. https://doi.org/10.3390/w14203254.
Müller Schmied, H., Trautmann, T., Ackermann, S., Cáceres, D., Flörke, M., Gerdener, H., Kynast, E., Peiris, T.A., Schiebener, L., Schumacher, M., Döll, P., 2024. The global water resources and use model WaterGAP v2.2e: description and evaluation of modifications and new features. Geosci. Model. Dev. 17, 8817–8852. https://doi.org/10.5194/gmd-17-8817-2024.
Muñoz-Sabater, J., Dutra, E., Agustí-Panareda, A., Albergel, C., Arduini, G., Balsamo, G., Boussetta, S., Choulga, M., Harrigan, S., Hersbach, H., Martens, B., Miralles, D.G., Piles, M., Rodríguez-Fernández, N.J., Zsoter, E., Buontempo, C., Thépaut, J.-N., 2021. ERA5-Land: a state-of-the-art global reanalysis dataset for land applications. Earth Syst. Sci. Data 13, 4349–4383. https://doi.org/10.5194/essd-13-4349-2021.
NASA Goddard Earth Sciences Data and Information Services Center (GES DISC), 2025. Global Land Data Assimilation System (GLDAS) Version 2.2. https://disc.gsfc.nasa.gov/datasets/GLDAS_CLSM025_DA1_D_2.2/summary (accessed 10 July 2026).
Ning, T., Feng, Q., Li, Z., Li, Z., Xi, H., Yang, L., Chang, X., 2023. Precipitation changes and its interaction with terrestrial water storage determine water yield variability in the world's water towers. Sci. Total. Environ. 880, 163285. https://doi.org/10.1016/j.scitotenv.2023.163285.
Panda, D.K., Ambast, S.K., Shamsudduha, M., 2021. Groundwater depletion in northern India: Impacts of sub-regional anthropogenic land use, socio-politics and changing climate. Hydrol. Process. 35, e14003. https://doi.org/10.1002/hyp.14003.
Pasik, A., Gruber, A., Preimesberger, W., De Santis, D., Dorigo, W., 2023. Uncertainty estimation for a new exponential-filter-based long-term root-zone soil moisture dataset from Copernicus Climate Change Service surface observations. Geosci. Model. Dev. 16, 4957–4976. https://doi.org/10.5194/gmd-16-4957-2023.
Prudhomme, C., Zsótér, E., Matthews, G., Melet, A., Grimaldi, S., Zuo, H., Garric, G., 2024. Global hydrological reanalyses: The value of river discharge information for worldwide downstream applications—the example of the Global Flood Awareness System GloFAS. Meteorol. Appl. 31, e2192. https://doi.org/10.1002/met.2192.
Rodell, M., Houser, P.R., Jambor, U., Gottschalck, J., Mitchell, K., Meng, C.-J., Arsenault, K., Cosgrove, B., Radakovich, J., Bosilovich, M., Entin, J.K., Walker, J.P., Lohmann, D., Toll, D., 2004. The Global Land Data Assimilation System. Bull. Am. Meteorol. Soc. 85, 381–394. https://doi.org/10.1175/BAMS-85-3-381.
Save, H., 2020. CSR GRACE and GRACE-FO RL06 Mascon Solutions v02. Center for Space Research, The University of Texas at Austin. https://doi.org/10.15781/cgq9-nh24.
Save, H., Bettadpur, S., Tapley, B.D., 2016. High-resolution CSR GRACE RL05 mascons. J. Geophys. Res. Solid. Earth 121, 7547–7569. https://doi.org/10.1002/2016JB013007.
Scanlon, B.R., et al., 2025. Multidecadal drought impacts on water storage in the Lower Colorado River Basin. Commun. Earth Environ. https://doi.org/10.1038/s43247-025-02149-9.
Scanlon, B.R., Zhang, Z., Save, H., Sun, A.Y., Müller Schmied, H., van Beek, L.P.H., Bierkens, M.F.P., 2018. Global models underestimate large decadal declining and rising water storage trends relative to GRACE satellite data. Proc. Natl. Acad. Sci. U. S. A. 115, E1080–E1089. https://doi.org/10.1073/pnas.1704665115.
Sen, P.K., 1968. Estimates of the regression coefficient based on Kendall's tau. J. Am. Stat. Assoc. 63, 1379–1389. https://doi.org/10.1080/01621459.1968.10480934.
Solovey, T., Śliwińska-Bronowicz, J., Janica, R., Brzezińska, A., 2025. Assessment of the effectiveness of GRACE observations in monitoring groundwater storage in Poland. Water Resour. Res. 61, e2024WR038888. https://doi.org/10.1029/2024WR038888.
Tapley, B.D., Bettadpur, S., Watkins, M., Reigber, C., 2004. The Gravity Recovery and Climate Experiment: Mission overview and early results. Geophys. Res. Lett. 31, L09607. https://doi.org/10.1029/2004GL019920.
Tapley, B.D., Watkins, M.M., Flechtner, F., Reigber, C., Bettadpur, S., Rodell, M., Sasgen, I., Famiglietti, J.S., Landerer, F.W., Chambers, D.P., Reager, J.T., Gardner, A. S., Save, H., Ivins, E.R., Swenson, S.C., Boening, C., Dahle, C., Wiese, D.N., Dobslaw, H., Velicogna, I., 2019. Contributions of GRACE to understanding climate change. Nat. Clim. Chang. 9, 358–369. https://doi.org/10.1038/s41558-019-0456-2.
Thomas, B.F., Famiglietti, J.S., Landerer, F.W., Wiese, D.N., Molotch, N.P., Argus, D.F., 2017. GRACE groundwater drought index: Evaluation of California Central Valley groundwater drought. Remote. Sens. Environ. 198, 384–392. https://doi.org/10.1016/j.rse.2017.06.026.
United Nations University Institute for Water, Environment and Health (UNU-INWEH), 2026. Global Water Bankruptcy: Living Beyond Our Hydrological Means in the Post-Crisis Era. United Nations University, Hamilton, Canada.
Usman, M., Qamar, M.U., Becker, R., Zaman, M., Conrad, C., Salim, S., 2020. Numerical modelling and remote sensing-based approaches for investigating groundwater dynamics under changing land use and climate in the agricultural region of Pakistan. J. Hydrol. 581, 124408. https://doi.org/10.1016/j.jhydrol.2019.124408.
van den Broeke, M., Bamber, J., Ettema, J., Rignot, E., Schrama, E., van de Berg, W.J., van Meijgaard, E., Velicogna, I., Wouters, B., 2009. Partitioning recent Greenland mass loss. Science 326, 984–986. https://doi.org/10.1126/science.1178176.
Velicogna, I., Sutterley, T.C., van den Broeke, M.R., 2014. Regional acceleration in ice mass loss from Greenland and Antarctica using GRACE time-variable gravity data. Geophys. Res. Lett. 41, 8130–8137. https://doi.org/10.1002/2014GL061052.
Vinca, A., Parkinson, S., Riahi, K., Byers, E., Siddiqi, A., Muhammad, A., Ilyas, A., Yogeswaran, N., Willaarts, B., Magnuszewski, P., Awais, M., Rowe, A., Djilali, N., 2021. Transboundary cooperation: A potential route to sustainable development in the Indus Basin. Nat. Sustain. 4, 331–339. https://doi.org/10.1038/s41893-020-00654-7.
Vörösmarty, C.J., Sahagian, D., 2000. Anthropogenic disturbance of the terrestrial water cycle. BioScience 50, 753–765. https://doi.org/10.1641/0006-3568(2000)050[0753:ADOTTW]2.0.CO;2.
Wang, L., Zhang, F., Shi, X., Zeng, C., Ahmad, I., Wang, G., Thapa, S., Xu, X., 2023a. Water resources system vulnerability in high mountain areas under climate change. J. Clean. Prod. 403, 136789. https://doi.org/10.1016/j.jclepro.2023.136789.
Wang, S., Cui, G., Li, X., Liu, Y., Li, X., Tong, S., Zhang, M., 2023b. GRACE satellite-based analysis of spatiotemporal evolution and driving factors of groundwater storage in the black soil region of Northeast China. Remote. Sens. 15, 704. https://doi.org/10.3390/rs15030704.
Wang, Z., Zhu, H., Chen, K., Li, M., Hu, S., Liu, J., Hu, Q., Sun, L., Gu, G., Li, H., 2026. Terrestrial water storage variations and drought characteristics in the Upper Yellow River Basin revealed by joint GNSS–GRACE analysis. J. Hydrol. Reg. Stud. 64, 103255.
Wiese, D.N., Landerer, F.W., Watkins, M.M., 2016. Quantifying and reducing leakage errors in the JPL RL05M GRACE mascon solution. Water Resour. Res. 52, 7490–7502. https://doi.org/10.1002/2016WR019344.
Yan, Y., Su, Y., Zhou, H., Wang, S., Yao, L., Batmunkh, D., 2025. Anthropogenic and climate-induced water storage dynamics over the past two decades in the China–Mongolia arid region adjacent to Altai Mountain. Remote. Sens. 17, 1949. https://doi.org/10.3390/rs17111949.
Yin, J., Slater, L.J., Khouakhi, A., Yu, L., Liu, P., Li, F., Pokhrel, Y., Gentine, P., 2023. GTWS-MLrec: Global terrestrial water storage reconstruction by machine learning from 1940 to present. Earth Syst. Sci. Data 15, 5597–5615. https://doi.org/10.5194/essd-15-5597-2023.

Zhu, H., Chen, K., Li, M., Hu, S., Zhang, G., Kuang, X., Cui, W., Zhang, S., Liu, J., 2025. Terrestrial water storage changes of Qinghai Lake on the Tibetan Plateau from joint inversion of GNSS and InSAR data. Water Resour. Res. 61 (6), e2024WR039503. https://doi.org/10.1029/2024WR039503.

Zhu, Y., Liu, S., Yi, Y., Xie, F., Grünwald, R., Miao, W., Wu, K., Qi, M., Gao, Y., Singh, D., 2021. Overview of terrestrial water storage changes over the Indus River Basin based on GRACE/GRACE-FO solutions. Sci. Total. Environ. 799, 149366. https://doi.org/10.1016/j.scitotenv.2021.149366.

Zou, H., Hastie, T., 2005. Regularization and variable selection via the elastic net. J. R. Stat. Soc. Ser. B Stat. Methodol. 67, 301–320. https://doi.org/10.1111/j.1467-9868.2005.00503.x.